HAL
open science

A New Alpine Metallogenic Model for the Pb-Ag Orogenic Deposits of Macôt-la Plagne and Peisey-Nancroix (Western Alps, France)

Maxime Bertauts, Emilie Janots, Magali Rossi, Isabelle Duhamel-Achin, Marie-Christine Boiron, Laura Airaghi, Pierre Lanari, Philippe Lach, Chantal Peiffert, Valérie Magnin

To cite this version:

Maxime Bertauts, Emilie Janots, Magali Rossi, Isabelle Duhamel-Achin, Marie-Christine Boiron, et al.. A New Alpine Metallogenic Model for the Pb-Ag Orogenic Deposits of Macôt-la Plagne and Peisey-Nancroix (Western Alps, France). Geosciences, 2022, 12 (9), pp.331. 10.3390/geosciences12090331 . hal-03766920v2

HAL Id: hal-03766920

https://brgm.hal.science/hal-03766920v2

Submitted on 20 Feb 2024

HAL is a multi-disciplinary open access archive for the deposit and dissemination of scientific research documents, whether they are published or not. The documents may come from teaching and research institutions in France or abroad, or from public or private research centers.

L'archive ouverte pluridisciplinaire **HAL**, est destinée au dépôt et à la diffusion de documents scientifiques de niveau recherche, publiés ou non, émanant des établissements d'enseignement et de recherche français ou étrangers, des laboratoires publics ou privés.

geosciences

MDPI

Article

A New Alpine Metallogenic Model for the Pb-Ag Orogenic Deposits of Macôt-la Plagne and Peisey-Nancroix (Western Alps, France)

Maxime Bertauts [1,*], Emilie Janots [1], Magali Rossi [2], Isabelle Duhamel-Achin [3], Marie-Christine Boiron [4], Laura Airaghi [5], Pierre Lanari [6], Philippe Lach [7], Chantal Peiffert [4] and Valérie Magnin [1]

1 Université Grenoble Alpes, Université Savoie Mont Blanc, CNRS, IRD, Université Gustave Eiffel, ISTerre, 38000 Grenoble, France
2 Université Savoie Mont-Blanc, CNRS, EDYTEM, 73000 Chambéry, France
3 BRGM, 13276 Marseille, France
4 Université de Lorraine, CNRS, GeoRessources, 54000 Nancy, France
5 Institut des Sciences de la Terre d'Orléans (ISTO), UMR 7327, CNRS-BRGM, Université d'Orléans, 45071 Orléans, France
6 Institute of Geological Sciences, University of Bern, 3012 Bern, Switzerland
7 BRGM, 45060 Orléans, France
* Correspondence: bertauts.maxime@gmail.com; Tel.: +33-64-688-6527

check for updates

Citation: Bertauts, M.; Janots, E.; Rossi, M.; Duhamel-Achin, I.; Boiron, M.-C.; Airaghi, L.; Lanari, P.; Lach, P.; Peiffert, C.; Magnin, V. A New Alpine Metallogenic Model for the Pb-Ag Orogenic Deposits of Macôt-la Plagne and Peisey-Nancroix (Western Alps, France). *Geosciences* **2022**, *12*, 331. https://doi.org/10.3390/geosciences12090331

Academic Editors: O. Adrian Pfiffner, Maria Iole Spalla, Gianni Balestro, Eduard Kissling, Olivier Lacombe and Jesus Martinez-Frias

Received: 29 June 2022
Accepted: 19 August 2022
Published: 31 August 2022

Publisher's Note: MDPI stays neutral with regard to jurisdictional claims in published maps and institutional affiliations.

Copyright: © 2022 by the authors. Licensee MDPI, Basel, Switzerland. This article is an open access article distributed under the terms and conditions of the Creative Commons Attribution (CC BY) license (https://creativecommons.org/licenses/by/4.0/).

Abstract: Understanding mass transfer associated with fluids circulation and deformation in the Alpine orogeny is often complex due to common multistage crystallization. For example, in two emblematic and historic Pb-Ag deposits of the French Alps, Macôt-la Plagne (MP) and Peisey-Nancroix (PN), a sedimentary or orogenic origin is still debated. To discriminate between the metallogenic models of the two deposits, an integrative methodology combining field, microstructural, mineralogical, thermobarometrical, and geochronological data was here applied for establishing detailed Pressure–Temperature–Time–Deformation (P-T-t-d) mineralization conditions. Both deposits are located in Permo-Triassic quartzite of the External Briançonnais domain along the Internal Briançonnais Front (Internal Western Alps). The ore mainly occurs as veins and disseminated textures containing galena, pyrite, and variable content of tetrahedrite–tennantite and chalcopyrite. Quartz porphyroclasts and sulfide microstructures indicate a dynamic recrystallization of the quartzite during the main fluid mineralization episode. Chlorites and K-white micas (phengite) chemical analysis and thermodynamic modeling from compositional maps indicate an onset of the mineralization at 280 °C, with a main precipitation stage at 315 ± 35 °C and 6.25 ± 0.75 kbar. In situ U-Pb dating on monazite, cogenetic with sulfides, gives ages around 35 Ma for both deposits. The integrative dataset converges for a cogenetic MP-PN Alpine Pb-Ag mineralization during deformation in relation to the thrusting of the "Nappe des Gypses" and the Internal Briançonnais at the metamorphic peak.

Keywords: Pb-Ag orogenic deposits; Western Alps; Briançonnais; U-Th-Pb geochronology; syn-tectonic mineralization; hydrothermal circulation; trace elements in sulfides; chlorite–phengite thermobarometry

1. Introduction

Fluids circulation associated with deformation in an orogenic context is at the origin of mass transfers, leading to the transport–deposition and remobilization of polymetallic deposits. Understanding metals' transfer and remobilization processes and scales is complex because deformation and fluids circulation are preferentially located at lithological contacts and on structures inherited from previous tectonic episodes. The French Alps present abundant polymetallic mineralizations that provide evidence of fluids circulation and significant mass transfer in the crust during successive orogenic cycles. Around 250 deposits and occurrences are identified by the BRGM (Bureau de Recherche Géologiques

et Minières) in the northern French Alps ("Armada" the GIS database of French metallic occurrences; available online http://infoterre.brgm.fr; accessed on 19 July 2019), mainly as Pb-Zn-Ag (44%) and Fe-Cu (29%) mineralizations, hosted in the Variscan basement, the Carboniferous and Permo-Triassic cover, and in the Liassic limestones (Figure 1) [1]. These polymetallic mineralizations were mainly investigated between the 1960s and 1980s, based mainly on the analysis of the structural context and petrographic analysis. Metallogenic models for most of these deposits are generally ambiguous, with no consensus on the geodynamic context that is proposed as late-Variscan (Sarrazins deposit; [2]), linked to Tethys Ocean opening (Macôt-la Plagne deposits; [3–5]) and to hydrothermal circulation during the Alpine collision (Macôt-la Plagne and Le Reveyret deposits; [6–8]). According to previous authors, e.g., [9–12], several mineralizations of the external crystalline massifs could result from previous mineralizations remobilized during the Alpine orogeny. In this study, we propose to evaluate the metallogenic models of two Pb-Ag deposits of the French Alps: the Macôt-la Plagne (MP) and Peisey-Nancroix (PN). These two ore deposits are emblematic as being among the most economically important Pb-Ag ore deposits in France during the 19th century. They are located in the same litho-structural context in Permo-Triassic phyllitic quartzite of the External Briançonnais domain of the Internal Alps. In the absence of ages or mineralizing conditions (P, T, speciation), metallogenic models are still debated because of the stratiform or vein-like type mineralizations that could either result from sedimentary or orogenic processes [3–8,13], as for other worldwide Pb-Zn(-Ag-Cu) deposits in several mountain belts (e.g., Pyrenees, Mount Isa region, and North China craton) mainly considered initially as sedimentary but revealed in fact to be orogen-driven [14–18]. This study proposes for the first time a multitechnique investigation on these two deposits, coupling field observations, microstructure and mineral paragenesis identification, and thermobarometry and geochronology. Based on recent success in determining the ages of Alpine clefts by the in situ dating of monazite (e.g., [19–21]), a special interest was set on monazite characterization in all the investigated samples. Thermobarometry was based on detailed chlorite–phengite characterization using compositional maps.

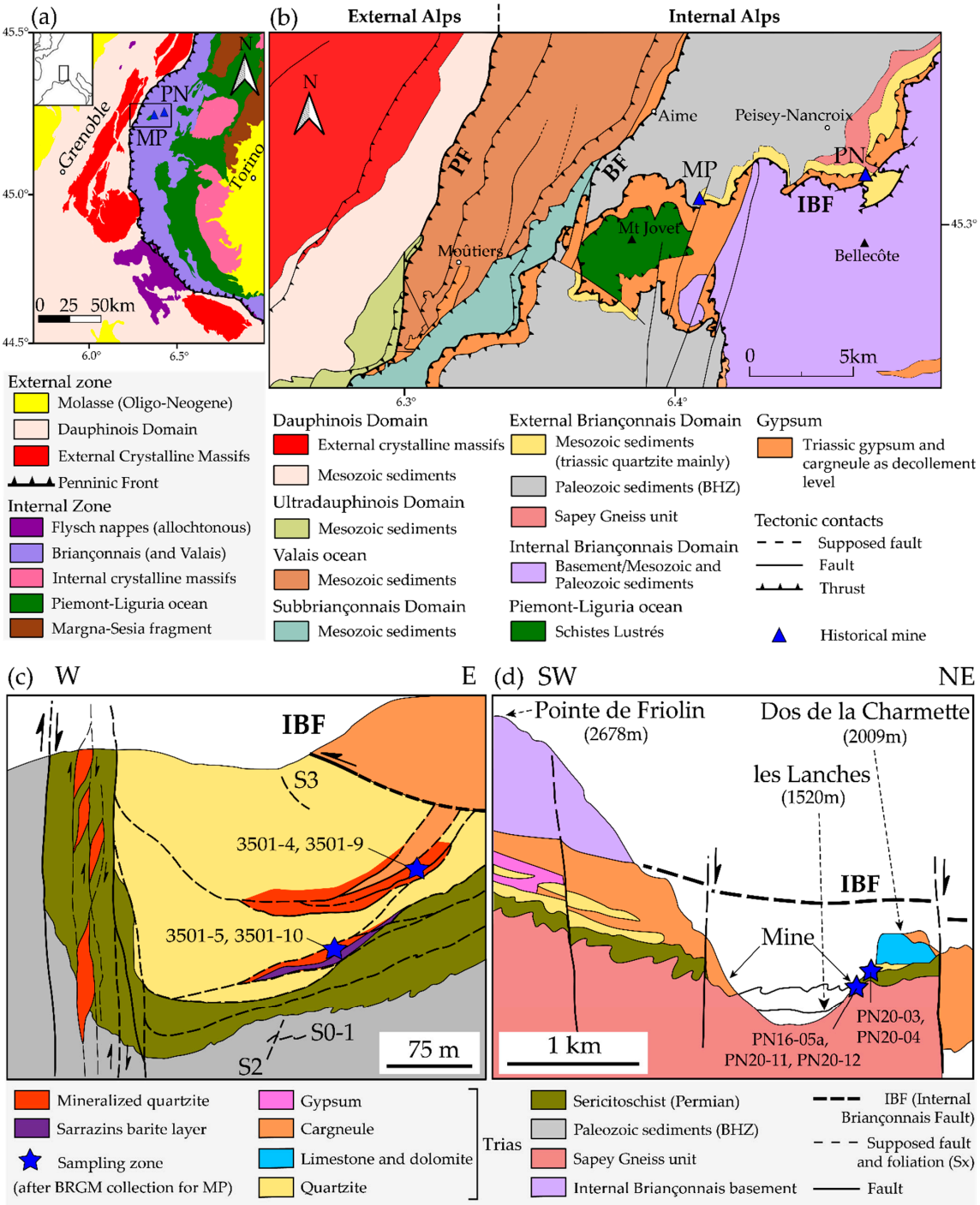

Figure 1. Geological map of (**a**) the Western Alps (after "Armada" France database) with square representing map b location; (**b**) the Briançonnais zone between the Lauzière and Vanoise massifs (modified after the Moûtiers geological map (1:50,000) by J. Debelmas). MP: Macôt-la Plagne; PN: Peisey-Nancroix; PF: Penninic Front; BF: Briançonnais Front; IBF: Internal Briançonnais Front. Additionally, sections modified after Guillot [22] of the (**c**) Macôt-la Plagne mine; and (**d**) Peisey-Nancroix valley. Sampling zones are given with the sample references. BHZ: Briançonnais Houiller Zone.

2. Geological Setting and Ore Mineralization

2.1. Regional Geology

The Peisey-Nancroix and Macôt-la Plagne mining sites are located in the Western Alpine arc, in the Briançonnais domain (Internal Alps, Figure 1a). The arrangement of the nappe pile shows a subduction-type structure in which most of the tectonic units dip southeastward. The current architecture of the Internal Alps results from the closure of the Valais and Piedmont-Liguria oceans (branches of the Alpine Tethys) during the Late Cretaceous and Cenozoic convergence between the European and African (Apulian/Adrian) tectonic plates. The Briançonnais domain corresponds to the continental margin located between both oceans, which was subducted under the African tectonic plates and thrust over the European tectonic plate during the alpine convergence (Figure 1a) [23]. The Internal metamorphic Alps are separated from the "unmetamorphic" External Alps by a major thrust called the Penninic Front, which delimits the onset of the collision of the European margin at around 35 Ma (Figure 1a,b) [24]. The External Alps correspond to the European margin; they comprise the Dauphinois and the Ultra Dauphinois domains. The Internal Alps consist of a stack of oceanic (Valais and Piedmont Schistes Lustrés nappes and associated ophiolites) and continental-margin-derived nappes (the Briançonnais domain and some pieces of the Adrian plate such as the Margna-Sesia fragments). The Briançonnais domain is divided into two units (the External and Internal Briançonnais) separated by the Internal Briançonnais Front (IBF). The IBF is a major detachment zone highlighted by a Late Triassic (Carnian) formation called the "Nappe des Gypses", which is composed of hundreds of meters (from 100 to 400 m) of dominant massive evaporites (mainly anhydrites), marine carbonates (dolomites tectonically transformed into cargneules), and shales and clays (metamorphosed into the Schistes Lustrés micaschists) (Barré et al. [25] and references therein). To the east of the IBF, the Internal Briançonnais is composed of Mesozoic sediments lying on top of a pre-Carboniferous metamorphic basement locally called the Vanoise-Mont Pourri unit. To the west of the IBF, the External Briançonnais is composed of the Variscan Sapey gneiss [26,27] and Carboniferous black schists containing anthracitic lenses, arkoses, and conglomerates, which are locally called the Briançonnais Houiller Zone (BHZ) [28,29]. This basement rock is overlain by a Permo-Triassic sedimentary cover represented by a series of schists, quartzites, limestones, and dolomites from bottom to top [30]. The External Briançonnais exhibits a low-grade alpine metamorphism, from lower greenschist facies to upper greenschist facies [31,32].

2.2. Structural Evolution of the Briançonnais Zone

The internal part of the Western Alpine arc experienced a complex and polyphase tectonic history. Precise dating highlights a diachronic tectono-metamorphic evolution, with a rejuvenation of the ages towards the west. In the External Briançonnais, Bertrand et al. [33] proposed three compressional stages (D1, D2 and D3 events), followed by a late extensional one.

1. The D1 event is characterized by an intense and penetrative schistosity (S1) oriented subparallel to S0 and by isoclinal folding. This early tectonic phase is interpreted as a top-to-the-northwest thrusting of the Internal Briançonnais over the External Briançonnais [34] (Lanari et al. [29] and references therein). The D1 deformation in the External Briançonnais occurred during the metamorphic peak. It is attributed to the exhumation of the Internal Briançonnais. There is no absolute age for the D1 deformation and metamorphic peak in the External Briançonnais. In the Internal Briançonnais, the D1 ranges from 55 and 43 Ma in the most internal parts [35,36] and until 35 Ma in the most external part (in the Modane-Aussois unit) [34]. The P-T conditions for D1 were constrained between 250–300 °C and 4–8 kbar in the BHZ [29], and 320–370 °C and 9–11 kbar in the cover of the Internal Briançonnais [34]. In the "Nappe des Gypses", the P-T conditions for the D1–D2 transition were estimated at 350 ± 20 °C and 6.5 ± 1.8 kbar using a $\delta^{18}O$ thermometer on carbonates [25].

2. The D2 event consists of a top-to-the-east shearing and thrusting highlighted by large-scale east-verging recumbent folds associated with the S2 schistosity, dipping to the west except into the eastern part of the BHZ. The D2 deformation occurred under greenschist facies conditions [37]. In the most internal part of the Briançonnais domain, the large-scale D2 shear zones are often parallel to S1 and interpreted as detachment faults related to extension [37]. The tectonic significance of the D2 event is still debated, as backthrusting [29,34,38–40] or as backfolding [41] during the continental collision, or as a detachment predating the continental collision [36,37]. Ages of backthrusting using $^{40}Ar/^{39}Ar$ and Rb-Sr dating on white mica are constrained between 35 and 32 Ma into the Internal Briançonnais [34,39]. The D2–D3 transition occurred at P-T conditions between 230–300 °C and 1–3 kbar in the "Nappe des Gypses" and Internal Alps sedimentary cover [25,34,36].
3. The D3 event is characterized by brittle structures and corresponds to the last stage of exhumation and to the formation of a large dome of crystalline basement associated with faulting in a brittle–ductile tectonic regime [36,37,42]. Bertrand et al. [33] suggest that the fan geometry of the BHZ results from the large-scale bending of the S2 schistosity due to D3 km-size folds. These D3 folds are associated with a sub-horizontal S3 schistosity (Lanari et al. [29] and references therein). This last D3 event is related to the last stage of exhumation below 300 °C during Oligocene-Miocene times with a southward tilting around an east–west axis into the Briançonnais zone [25,29,34].

2.3. The Pb-Ag Mining District of Macôt-la Plagne (MP) and Peisey-Nancroix (PN)

The investigated Pb-Ag deposits of Macôt-la Plagne (MP) and Peisey-Nancroix (PN) are located in the Vanoise massif, at the contact of the Permo-Triassic External Briançonnais with cargneules (Figures 1 and 2a). Cargneules are Triassic dolomites that have been brecciated and partly dissolved during the alpine orogeny from sulfate-rich fluids derived from Triassic gypsum. In the studied area, cargneules can be related to the "Nappe des Gypses", and therefore to the Internal Briançonnais Fault (IBF; Figure 1b). Both deposits are hosted in Triassic (Werfenian stage) quartzite (tQ on Figure 2a) and Permian sericite schists and phyllitic quartzite (rt on Figure 2a). The MP ore deposit is located within a recumbent dissymmetrical syncline, with a NNE/SSW axis (Figure 1c) [43]. The PN deposit is bordered by two faults: the Mine Fault (M.F.) and the IBF (Figure 2a). The IBF is described as the thrusting of the Internal Briançonnais (Vanoise massif in the study zone) on top of the External Briançonnais, while the Mine Fault is a detachment level of the allochthonous External Briançonnais cover on the basement. In the study area, the IBF is characterized by two successive faulting activities, first with a top-to-the-west horizontal thrusting, followed by vertical normal faulting with a likely sinistral shearing component [43].

The Pb-Ag mines of MP (main exploitation: 1810–1973) and PN (exploitation: 1734–1866) were the most economically important of the French Alps. The historical production is estimated at 125,600t of Pb and 360t of Ag (with an average content of 3.7% of Pb and 0.015% of Ag) and 22,000 t of Pb and 53 t of Ag, for MP and PN, respectively, with a peak of activity during the 19th century [1,3,44,45]. In both deposits, the ore is characterized by Ag-rich galena, either massive or disseminated in a quartz- or barite-rich gangue. Tetrahedrite and pyrite are systematically associated with galena, with variable chalcopyrite, arsenopyrite, sphalerite, and bournonite [6,13,46,47]. Fluorite was never reported for these deposits.

Waline [7] describes three types of ores for the Macôt-la Plagne deposit (Figure 1c): (1) the Charles-Albert-type Pb-Ag veins, consisting of mineralized quartzite intercalated within the Permian schists, forming discontinuous lenses; (2) the Sarrazins-type veins, with banded fine-grained galena and barite; (3) pods-type ore, with well-crystallized galena hosted in mylonitic quartzite. The mineralization is well-aligned along the schistosity, with no particular relationship between the mineralization and the Permian schist-Triassic quartzite contact.

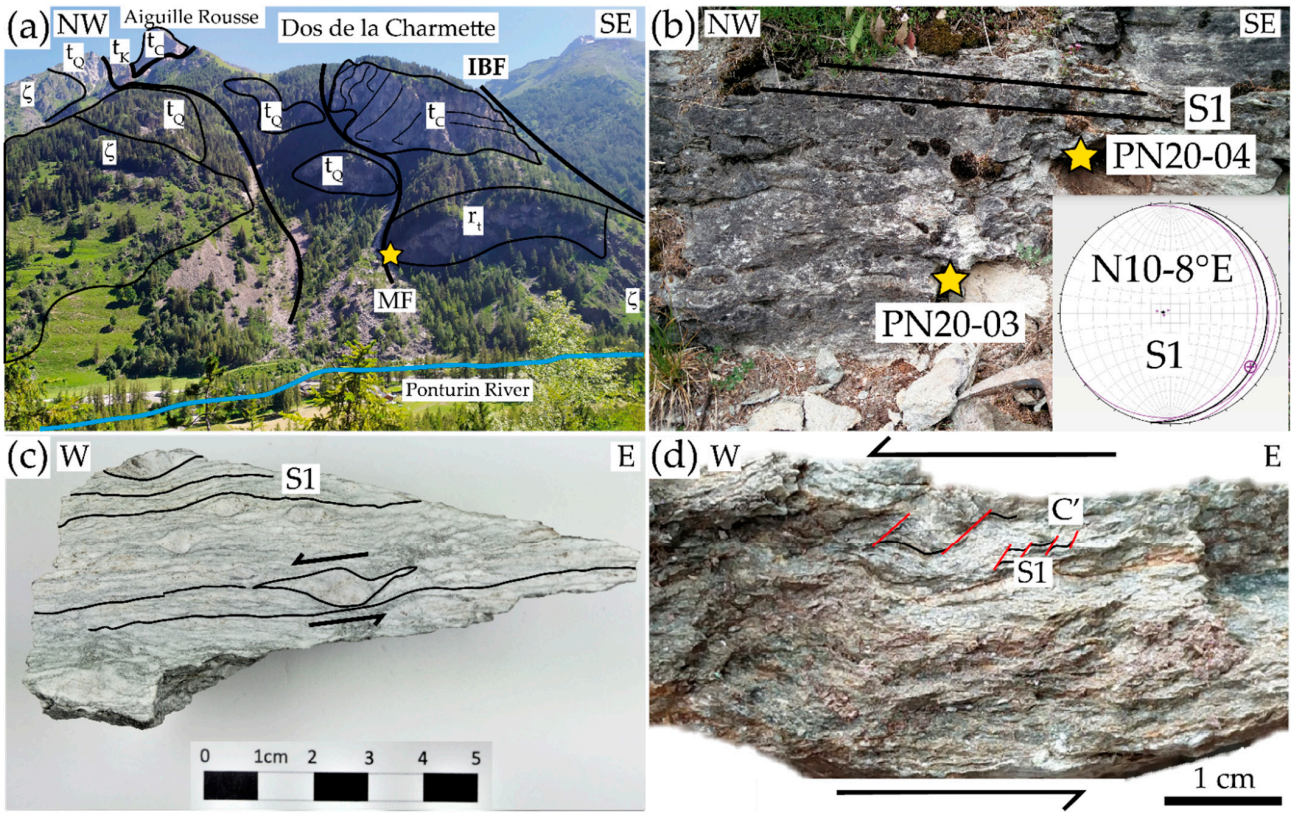

Figure 2. (**a**) Photo of the Peisey-Nancroix valley (PN on the Figure 1b), Ponturin River right bank with outcrop location b (yellow star), and (**b**) outcrop of Permian schist and quartzite (rt) with the stereonet of the S1 schistosity and samples location (yellow stars). (**c**,**d**) Photo of the two samples from the PN outcrop showing a top-to-the-west kinematic of deformation: (**c**) Mylonitic quartzite with the schistosity highlighted by phyllite and the direction given by deformed porphyroclast of quartz (PN20-03); (**d**) Schist with shear planes (red line; C′) transecting the main schistosity (S1) at an angle of about 30–60° (PN20-04). ζ: Sapey gneiss; rt: Permian schist and phyllitic quartzite; tQ: Triassic quartzite; tC: Triassic carbonates; tK: Triassic evaporites; M.F.: Mine Fault.

3. Field Description, Structural Analyses, and Sampling

3.1. Field Description and Structural Analyses

For the PN deposit, the main expressed foliation in the Permian and Triassic rocks (S1) is subhorizontal and dips to the east at the contact with the Mine Fault (M.F., Figure 2a,b). The coarse lineation is roughly NW-SE oriented. In the Permian mylonitic phyllitic quartzite (PN20-03, Figure 2c), the S1 foliation is highlighted by fine-grained white micas. Porphyroclasts of deformed quartz indicate a top-to-the-west kinematic. The C′-type shear bands are short, anastomosing, and wavy, and cross-cut the S1 mylonitic schistosity at relatively high angles (Passchier and Trouw [48] and references therein). The direction of deformation observed in the phyllitic quartzite is consistent with the C′-type shear bands structure dipping westward, shown by the Permian sericite schist (PN20-04, Figure 2d). S2 foliation was only observed to affect the pervasive S1 foliation as isoclinal folds on the other side of the Ponturin River.

3.2. Samples

The entrances of the two abandoned mines are sealed and no longer accessible for in situ structural observations or sampling. Four samples from the MP deposit were selected from Raguin's historical collection, which is kept by BRGM (Orléans, France). The samples come from two mineralized districts within Triassic quartzite: the Quartzite Est and the Sarrazins Districts. In the former district, a massive sulfide was selected from vein 0/8

(3501-9) and a disseminated ore from vein 0/10 (3501-4). Similarly, a massive sulfide (3501-10) and a more disseminated ore showing millimetric veins (3501-5) were selected from the Sarrazins District (Figure 1c). For the PN deposit, three samples were collected on a mine waste heap (Figure 1d). The mineralization occurs in veins or impregnation within mylonitic phyllitic Triassic quartzite (PN16-R05a, PN20-11, PN20-12).

4. Analytical Methods

4.1. Petrographical Observations

A detailed petrographic study was carried out at ISTerre using an optical microscope combined with back-scattered-electron imaging using a scanning electron microscope (SEM) Tescan Vega 3 in order to identify the mineralogical parageneses, including the sulfides–sulfosalts, the gangue, and accessory minerals. Particular attention was paid to micrometric minerals inclusions and possible compositional zoning in the back-scattered-electron images.

4.2. Sulfides–Sulfosalts EPMA and LA-ICP-MS Trace Elements Protocols

Major and minor element analyses were performed using a JEOL JXA-8230 electron microprobe (EPMA) at ISTerre (Grenoble, France) equipped with five wavelengths dispersive spectrometers. Quantitative point analyses were made at 20 keV and 50 nA. The following 15 elements, standards, analytical lines, and monochromators were used for measurements: S (PbS, Ka, PETH), Cu (CuFeS2, Ka, LiFH), Fe (CuFeS2, Ka, LiFH), Pb (PbS, Ma, PETH), Zn (ZnS, Ka, LiFH), Sb (Sb, La, PETH), Ag (Ag, La, PETH), Cd (CdS, Lb, PETH), Sn (SnO2, La, PETH), Mn (MnSiO3, Ka, LiFH), Hg (HgS, La, LiFL), Co (CoO, Ka, LiFL), Ni (Ni, Ka, LiFL), As (FeAsS/InAs, La, TAP for galena and Ka, LiFL for chalcopyrite/tetrahedrite–tennantite), and Bi (Bi, La, LiFL for galena and Ma, PETH for chalcopyrite/tetrahedrite–tennantite). Peak counting times were scaled from 40 to 400 s for a total point analysis time of 400 s. Internal JEOL procedures were used for data reduction (i.e., quantification of element contents, uncertainties, and limits of detection). Measurements were collected on 3501-5a, 3501-9b, and PN16-R05a thin sections (30 µm). Among the 15 elements monitored, Co, Mn, Ni, and Bi were not measured, as well as As for galena, and Cd and Hg for chalcopyrite. Nonetheless, trace element analyses using EMPA are limited due to the compromise between the counting time, the number of measured elements, and the required limits of detection. Conditions for X-ray maps in the tetrahedrite grains from the PN16-R05a sample were fixed at 20 keV, 100 nA, dwell time of 200 ms, for a surface area of 300 × 360 µm with a step of 1 µm.

Trace element analyses in sulfides were carried out using Laser Ablation Inductively Coupled Plasma Mass Spectrometry (LA-ICP-MS) at the GeoRessources laboratory (Vandoeuvre-lès-Nancy, France), equipped with an ESI New Wave Excimer laser (193 nm) coupled with the Agilent 7900 quadrupole ICP-MS. Laser ablation conditions were fixed at 5Hz pulse rate, 6 mJ/cm^2 laser energy, 200 laser pulses. Selected zones of the minerals were ablated with 60 µm spot diameter from the 3501-9b, 3501-10a, PN20-11, and PN20-12 150 µm-thick sections. The ablated material was transported using a constant He flows (700 mL/min) and mixed with Ar (0.85l/min) in a cyclone coaxial mixer prior to entering the ICP torch and being ionized. Data were collected during a 30 ms dwell time per channel to enhance the number of counts for trace elements. The following isotopes were monitored: ^{34}S, ^{52}Cr, ^{55}Mn, ^{57}Fe, ^{59}Co, ^{60}Ni, ^{63}Cu, ^{66}Zn, ^{71}Ga, ^{74}Ge, ^{75}As, ^{82}Se, ^{95}Mo, ^{107}Ag, ^{111}Cd, ^{115}In, ^{118}Sn, ^{121}Sb, ^{125}Te, ^{197}Au, ^{202}Hg, ^{205}Tl, ^{208}Pb, and ^{209}Bi. All elements were measured with an integration time of 20 ms, except ^{34}S, ^{57}Fe (10 ms), ^{197}Au, and ^{205}Tl (30 ms). The ^{74}Ge was chosen over ^{72}Ge following the study of interferences from Bellissont et al. [49]. External standard calibration was performed with the synthetic polymetallic sulfide material MASS-1 [50]. Data reduction was carried out using Iolite software (version 4) [51], following the standard methods of [52], and using Pb or Cu content—known from prior EPMA analyses (in same grains or averaged grains from the same location)—as

an internal standard for galena, chalcopyrite, and tetrahedrite–tennantite solid solution, respectively.

4.3. Chlorite–Phengite EPMA Protocol and Thermometry Calculation

All investigated samples contain white mica (phengite). From the 7 rock samples investigated (Supplementary Table S1), the only MP sample containing both chlorite and phengite was selected for geothermobarometry (3501-5b). No chlorite was found in samples from the PN deposit. Comparison of the chemistry of phengite from the matrix with phengite in inclusions was performed on sample PN16-R05a, which was the most precisely investigated and the only one showing a poikilitic texture. Chemical compositions of chlorite and phengite were determined by point analyses and X-ray maps with electron microprobe analyses using a JEOL JXA-8230 at ISTerre. Quantitative point analyses were made at 15 keV and 10 nA. Conditions for X-ray maps in the selected sample 3501-5b were fixed at 15 keV, 100 nA, dwell time of 200 ms, for a surface area of 310 × 300 µm with a step of 0.5 µm. Raw X-ray maps were converted into oxide wt% maps using point analyses measured on the map area as internal standards [53] with the software XMapTools 3.4.1 [54,55]. Structural formulae were then calculated for each pixel on a 14-oxygen basis and 11-oxygen basis for chlorite and phengite, respectively.

Chlorite analyses that did not satisfy the following criteria were rejected: (i) Alkali sum (K_2O + Na_2O + CaO) < 1 wt% [56,57], and (ii) Octahedral sum (Al^{VI} + Fe + Mn + Ca + Na + K) $\leq$ 6 apfu. Phengite analyses that did not satisfy the following criteria were rejected (following Parra et al. [58]): (i) 92 wt% $\leq$ Oxygen sum $\leq$ 96 wt%; (ii) TiO_2 + MnO + CaO < 0.5 wt% and (iii) Alkali sum $\geq$ 0.9 apfu. The K-mica–quartz–water thermodynamic model of Dubacq et al. [59] allows modeling K-mica compositional variation as a function of temperature and pressure.

The temperature range of chlorite growth was calculated for each pixel of the chlorite compositional map using the chlorite–quartz–water thermometer of [60–62] with individual estimation of the Fe^{3+}/Fe_{tot} (XFe^{3+}). Pressure was fixed at 5 kbar, water activity at 1, and the minimum XFe^{3+} at 10% to avoid the overestimation of temperature highlighted by Lanari [63], especially for HT (>350 °C)-LP (<5 kbar) chlorite. An average temperature was calculated from chlorite zones using a Monte Carlo technique (3000 iterations for each pixel) to test the temperature distribution. Conventional empiric thermometer based on the Al^{IV} content of chlorite [64] was also applied for comparison.

The temperature range of phengite growth was estimated using the phengite–quartz–water thermometer of Dubacq et al. [59]. The equilibrium conditions of K-mica–quartz–water were represented by a P-T line along which the water content varies. The thermodynamic model of Dubacq et al. [59] was also used for pressure estimates at fixed temperature values (see Lanari et al. [29]).

4.4. Monazite Composition Analysis and Dating (EPMA and LA-ICP-MS)

Monazite chemical compositions were analyzed using a JEOL JXA-8230 electron microprobe at ISTerre to unravel intragrain zoning on the PN16-R05a and 3501-5b thin sections. The X-ray maps were acquired at 15keV and 100nA, and 1000 ms dwell time for a surface area of 170 × 55 µm and using 1 µm step on a PN16-R05a monazite grain. Quantitative point analyses of the monazite were obtained using a 15keV and 200nA beam modified after Scherrer et al. [46]. From U, Th, and Pb concentrations, a chemical age was then calculated using NiLeDAM software [65,66] with an age uncertainty at 2σ. All analyses with SiO_2 content > 1 wt% (contamination from surrounding silicates) or Pb detection below the detection limit of around 100 ppm were not taken into account.

In situ monazite U-Pb isotopic dating was done on one PN (PN16-R05a) and three and MP thin sections (3501-4a, 3501-5b, and 3501-10a) using the LA-ICP-MS at the BRGM (Orléans, France). The mass spectrometer is an ICP-MS X series II set up in Xs lenses coupled with a Cetac Excite 193 nm laser at short timing pulse. The sample was placed in a double-volume cell swept by a helium flux (analysis conditions are summarized in

Supplementary Table S2). Analyses were normalized to the Trebilcock monazite (272 ± 2 Ma) [67] with a quality control on the Madmon standard monazite (523 ± 12 Ma) [68]. Reduction data was done using the Glitter© software. The ^{235}U contents were recalculated from measured contents of ^{206}Pb, ^{207}Pb, and ^{238}U using the disintegration equation. The age calculation was performed using IsoplotR on R [69] with a standard deviation of 2σ, and the isochron was drawn using an ordinary least squares regression. A size spot of 10 or 15 µm was chosen to maximize the signal. For the PN deposit, the analyses which statistically diverge from the Discordia line have been removed from the age calculation. A SEM control was then realized for the 6 removed analyses, providing evidence of interference as inclusions or mineral interfaces.

5. Petrographic Results

The MP and PN Pb-Ag deposits show significant similarities in terms of microstructure, ore mineralization, and mineral assemblages. Consequently, a unique petrogenetic sequence is proposed for the two deposits.

5.1. Sample Microstructures

The MP and PN Pb-Ag deposits correspond to mineralized quartzite and to phyllitic quartzite (1 to 15% white mica; Figure 3) with intergranular disseminated mineralization along the foliation, millimetric to pluricentimetric veins, and massive sulfides (Figure 3).

Samples with a disseminated texture have a mylonitic fabric consisting of quartz porphyroclasts surrounded mainly by galena and phengite (Figures 3 and 4). Submillimetric to millimetric anhedral quartz porphyroclasts (Qz1) are elongated along the stretching lineation (Figures 3c and 4a,c). They exhibit undulose extinction and are replaced and surrounded by recrystallized equigranular and isometric grains with a micrometer size (Qz2). Relics of Qz1 porphyroclasts show pervasive intragranular fractures at high angles to the foliation that can be healed with trails of fluid inclusions or sealed by Qz2 with some minor sulfide–sulfosalts (mainly galena; Figure 4a,c). Newly formed Qz2 and sulfide–sulfosalts assemblages (galena, pyrite, tetrahedrite–tennantite, and chalcopyrite) can also occur in dilatation zones that crosscut the healed microcracks (Figure 4b), or in strain shadows of Qz1 (Figure 4a,b). In some places, Qz1 is completely replaced by Qz2 associated with sulfides, but the Qz1 porphyroclasts (or Qz1 porphyroclast aggregates) initial shape is preserved and molded by phengite and sulfides (Figures 3f and 4c,d). Apart from quartz, phengite is the second main silicate associated with the mineralization. Phengite occurs as micrometric acicular grains oriented within the S1 foliation (Figures 3c and 4), but it also sometimes appears as randomly oriented and folded aggregates up to 100 µm in size.

5.2. Paragenetic Sequence

The ore is mainly made of galena with variable amounts of pyrite, tetrahedrite–tennantite, and chalcopyrite, and rare arsenopyrite, cobaltite–gersdorffite, sphalerite, and bournonite (Figures 3–5). In samples with a massive texture, galena contains relics of Qz1 porphyroclasts recrystallized into Qz2, pyrite, and rare gypsum (Figure 3b,f) associated with fractured dolomite (Figure 3b). In disseminated texture, sulfides–sulfosalts occur mostly within the foliation between quartz and phengite (Figure 4c,d) or in millimetric to centimetric sulfide veins parallel or perpendicular to the foliation often intergrown with tetrahedrite–tennantite, pyrite, or chalcopyrite (Figures 3a,c,e and 4e,f). In these samples, galena may occur as fine-grained intergrowth (displaying 120° triple-junction grain boundaries; Figure 5f) with tetrahedrite–tennantite, chalcopyrite, pyrite, barite, and dolomite–ankerite (Dol-Ank), displaying sector zoning with variable Mg, Fe, and Mn contents (Figures 3e and 8a), quartz, monazite, and phengite (Figures 3b, 4e,f and 5). Apart from galena, pyrite can be abundant within some veins. Galena, monazite, barite, and dolomite can be found in inclusions within pyrite (Figure 5e,f). Generally, PN samples contain more abundant tetrahedrite–tennantite compared to MP, where this mineral is

rare. In contrast, the MP deposit contains abundant barite, which is rarely represented in PN. One sample from PN shows peculiar features, such as (i) a poikilitic texture with abundant inclusions of quartz and phengite found in sulfides and sulfosalts, and (ii) the presence of microspheres of florencite (a REE-aluminophosphate) in sulfides–sulfosalts, Qz2 micrograins, and phengite (Figure 5c). The entire description above is resumed in the paragenesis presented in Figure 6.

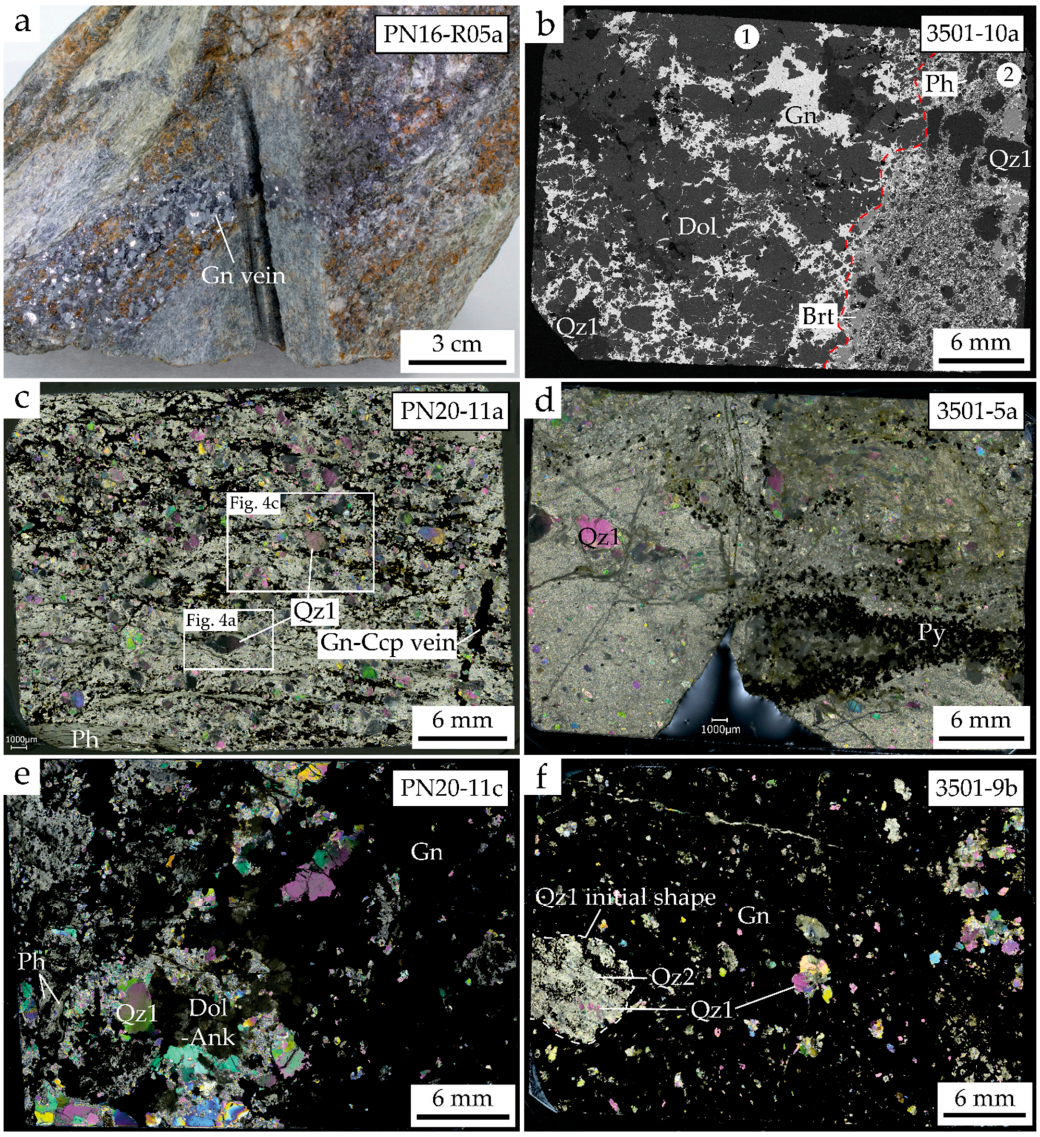

Figure 3. Macroscopic views of rock samples (**a**); BSE thin section image (**b**); thick sections under cross polars (**c**–**f**) of the various typologies of the Pb-Ag ore. (**a**) Massive galena in a vein crosscutting a phyllitic quartzite from a mining waste of the Peisey-Nancroix mine (PN16-R05a). (**b**) Fractured dolomite filled mainly by massive galena (zone 1) at the contact with fine-grained tetrahedrite–tennantite, galena, pyrite, and gangue (barite, quartz, and phengite) (zone 2) in MP sample (3501-10a). Note the deformed porphyroclasts of quartz with some chlorite in 3501-10. Images of thick sections from: (**c**) Thick section of quartzite with disseminated ore aligned in the schistosity (PN20-11a); (**d**) Quartzite with pyrite-carbonates veins (3501-5a); (**e**) Quartzite with massive ore (PN20-11b); (**f**) Massive sulfides with quartz porphyroclasts (3501-9b). Brt: barite; Ccp: chalcopyrite; Chl: chlorite; Dol: dolomite; Dol-Ank: dolomite–ankerite; Gn: galena; Py: pyrite; Qz: quartz (after Whitney and Evans [70]).

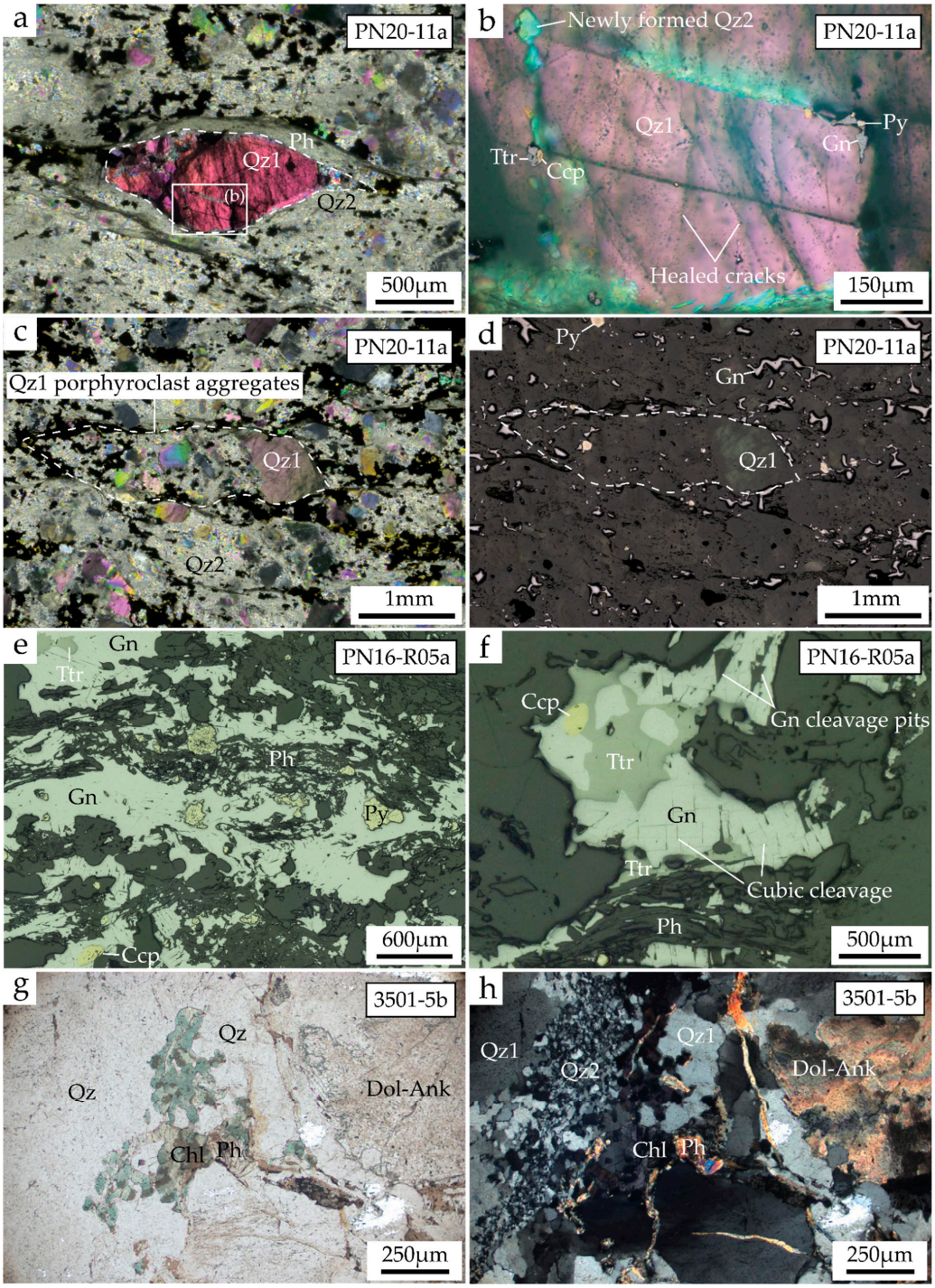

Figure 4. Examples of microstructures observed using optical microscopy. (**a**) Deformed Qz1 porphyroclast along the main foliation, surrounded and molded by micrometric phengite oriented in the foliation, and equigranular micrograins of Qz2 (thick section, PN20-11a, polarized light); (**b**) Microfractures healed and sealed by recrystallized Qz2 and sulfide–sulfosalts in a Qz1 porphyroclast (zoom of image a, polarized and reflected lights). Note that healed microcracks are cut off by newly formed Qz2 and sulfide–sulfosalts. (**c**,**d**) Qz1 porphyroclasts variably recrystallized in isometric and equigranular Qz2 micrograins and sulfides (galena and pyrite) in polarized light (**c**) and reflected light ((**d**); PN20-11a; thick section). Note that, when absent, the initial shape of Qz1 porphyroclast is

evidenced by galena and phengite delineation (white dashed line). (**e**) Galena and phengite aligned into the main foliation with inclusions of subeuhedral pyrite, tetrahedrite–tennantite and chalcopyrite inside galena (PN16-R05a thin section, reflected light); (**f**) Anhedral galena with typical cubic and triangular pit cleavages, intergrown with chalcopyrite (PN16-R05a thin section, reflected light). (**g**,**h**) Euhedral chlorite and phengite surrounded by deformed and recrystallized quartz nonpolarized light (**g**) and polarized light ((**h**); 3501-5b thin section). Ccp: chalcopyrite; Chl: chlorite; Dol-Ank: dolomite–ankerite Gn: galena; Ph: phengite; Py: pyrite; Qz: quartz; Ttr: tetrahedrite–tennantite solid solution.

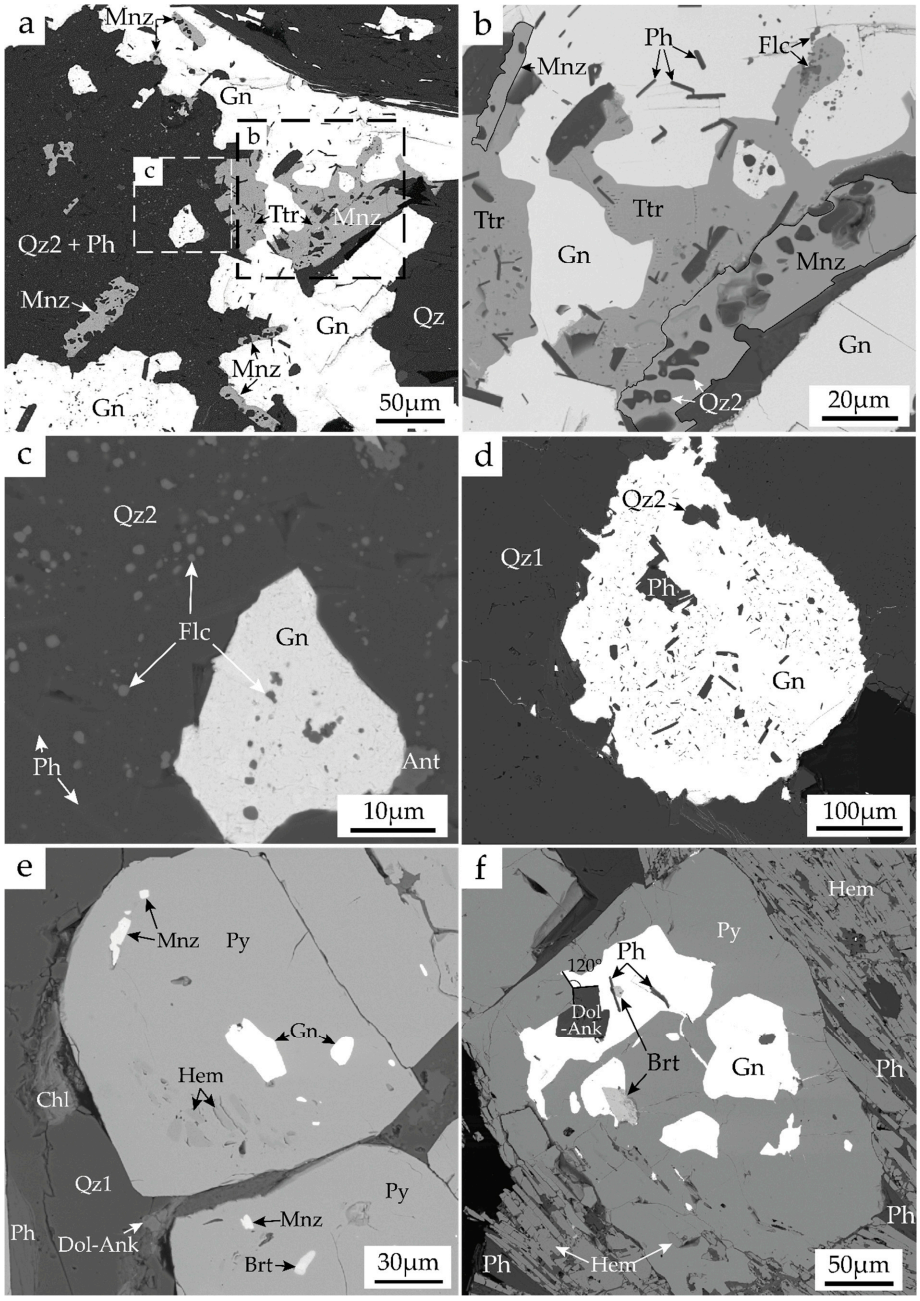

Figure 5. Backscattered electron (BSE) images of sulfides–sulfosalts from PN (PN16-05a; (**a**–**d**)) and MB (3501-5b; (**e**,**f**)) ores. (**a**) Galena and tetrahedrite hosted in quartz and phengite matrix (PN16-R05a), dashed squares show the location of (**b**,**c**) images. Note (i) monazite inclusions within galena and the intergrowth between galena, tetrahedrite, and monazite; (ii) the poikilitic texture of monazite

and sulfides–sulfosalts with similar inclusions of Qz2 micrograins, acicular phengite, and spherical florencite. (**b**) Intergrowth textures between galena, tetrahedrite, and monazite and the occurrence of florencite inclusions within phengite, tetrahedrite, and monazite; (**c**) Florencite inclusions within the Qz2 micrograins and phengite matrix; (**d**) Inclusion-free galena observed at the rims and filling fractures of inclusion-rich galena; (**e**) Inclusions of monazite, galena, hematite, and barite within pyrite; (**f**) Inclusions of galena, barite, dolomite, hematite, and phengite within pyrite (also note the ≈120° triple-junction grain boundaries between galena, dolomite, and pyrite). Ant: anatase; Brt: barite; Chl: chlorite; Dol: dolomite–ankerite; Flc: florencite; Hem: hematite; Mnz: monazite Gn: galena; Ph: phengite; Py: pyrite; Qz: quartz (after Whitney and Evans [70]).

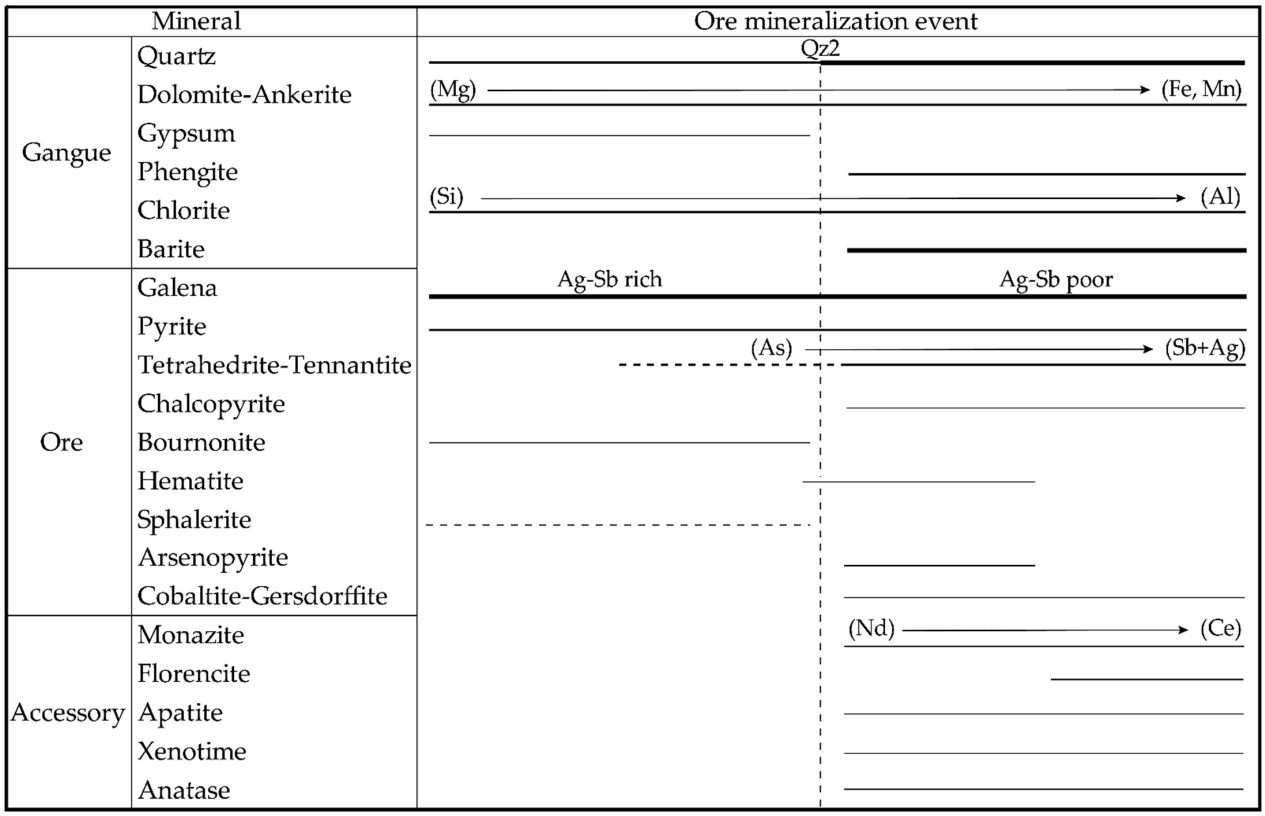

Figure 6. A common paragenesis for the Macôt-la Plagne and the Peisey-Nancroix Pb-Ag deposits. The thickness of the line represents the proportion of each phase.

6. Sulfides and Sulfosalts Trace Element Composition

Trace elements were investigated first using EPMA and then LA-ICP-MS. Sulfides–sulfosalts trace element compositions are summarized in Table 1. For galena, the trace elements are generally below the EPMA detection limits, except for Ag and Sb. With LA-ICP-MS, variations in Ag, Sb, Bi, Tl, Cd, As, Sn, Mn, Fe, Hg, and Cr contents are detected, while Te, Au, Mo, Ge, and Ga contents remain below the detection limits. The MP galena (3501-5a, 3501-9b, and 3501-10a) shows a significant correlation between Ag (480–1665 ppm) and Sb (580–2080 ppm) concentrations (Figure 7), which attests for a coupled substitution of these elements (George et al. [71] and references therein). The highest Ag and Sb contents are only observed within the massive galena texture of 3501-9b. In 3501-10a (Figure 3b), massive galena within the dolomite fractures (zone 1) exhibit slightly lower to similar Ag and Sb contents than the massive galena (3501-9b. Opposite, the fine-grained galena (zone 2) has much lower Ag-Sb contents. Galena from the PN samples (PN16-R05a, PN20-11 and PN20-12) displays low Ag (<540 ppm) and Sb (<700 ppm) contents, similar to the lower Ag-Sb contents from the disseminated MP samples (3501-5b and 3501-10a zone2; Figure 7). The Bi content in the PN galena (up to 60 ppm) is

significantly higher than in the MP galena (<1 ppm), especially in vein-type galena. Both the MP and PN galena analyses are aligned along the main coupled substitution: $Ag^{+} + (Sb + Bi)^{3+} \rightarrow 2Pb^{2+}$. The microprobe analyses display the same correlation between the Ag-Sb-rich galena (3501-9b) and Ag-Sb-poor galena from the vein-type mineralization (3501-5a and PN16-R05a; Figure 7). They also show a slightly richer Ag-Sb galena in larger veins (PN16-R05a; Figure 3a) compared to millimetric veins (PN20-11; Figure 3c). Variations of Mn, Fe, and Hg (up to 3100 ppm for Fe in one analysis) are not correlated with other trace elements. Cd and Cu show content variation mainly ranging from 1 to 100 ppm, with rare concentrations up to 400 ppm.

Table 1. Sulfides–sulfosalts major element concentrations determined by EPMA in wt%, and trace elements by LA-ICP-MS in ppm.

Mineral	Sample	Pb (wt%)	Cu	Fe	Zn	As	Ag	Sn	Sb	Bi
Galena	**3501-5a** *									
	Min.	85.31	-	-	-	-	260	-	369	-
	Max.	86.93	-	179	-	-	1003	152	912	-
	Mean (17)	86.2	-	20	-	-	588	8.9	548	-
	1σ	0.52	-	56	-	-	175	37	160	-
	3501-9b									
	Min.	86.52	1.3	0.2	1.1	16	1340	0.2	1670	0.1
	Max.	87.17	19	11	1.6	37	1665	0.4	2081	0.9
	Mean (13)	**86.8**	9.8	3.6	1.3	30	1507	0.2	1866	0.4
	1σ	0.33	4.3	4.3	0.3	5.8	92	0.1	125	0.2
	3501-10a									
	Min.		0.6	1.1	0.4	3.0	481	0.2	585	0.1
	Max.	**86.0**	18	3113	5.3	16	1447	0.3	1729	0.5
	Mean (11)		8.9	493	1.9	13	957	0.2	1165	0.3
	1σ		6.8	1157	1.5	4.0	374	0.0	446	0.1
	PN16-R05a *									
	Min.	85.49	-	-	-	-	369	-	277	-
	Max.	86.53	-	203	-	-	537	-	694	-
	Mean (5)	86.0	-	41	-	-	449	-	524	-
	1σ	0.39	-	91	-	-	68	-	156	-
	PN20-11									
	Min.		229	0.5	0.1	38	246	0.3	245	9.2
	Max.	**86.0**	259	249	0.9	40	369	0.7	416	55
	Mean (6)		244	53	0.5	39	297	0.5	314	30
	1σ		22	110	0.5	1.0	48	0.2	62	22
	PN20-12									
	Min.		-	1.5	0.7	17	174	0.9	111	12
	Max.	**86.0**	66	26	3.6	75	328	2.0	289	61
	Mean (14)		6.9	8.4	1.5	38	240	1.2	191	31
	1σ		21	9.7	0.9	22	47	0.3	47	19

Mineral	Sample	Pb	Cu (wt%)	Fe (wt%)	Zn (wt%)	As (wt%)	Ag (wt%)	Sn	Sb (wt%)	Bi
Tetrahedrite –Tennantite	PN16-R05a *									
	Min.	-	32	2.8	3.8	3.2	5.3	1132	21	-
	Max.	-	35	3.5	4.4	5.6	6.7	1370	25	-
	Mean (10)	-	34	3.1	4.1	4.5	6.1	1232	23	-
	1σ	-	0.9	0.2	0.2	1.0	0.4	100	1.5	-
	PN20-12									
	Min.	0.3		2.2	6.2	20	1.2	0.1	3.8	0.8
	Max.	2.4	**35.0**	2.3	6.3	23	1.5	2.5	5.2	2.5
	Mean (5)	1.4		2.2	6.3	22	1.3	0.6	4.7	1.3
	1σ	0.8		0.1	0.1	1.5	0.1	1.1	0.6	0.7

Mineral	Sample	Pb	Cu (wt%)	Mn	Fe (wt%)	Zn	As	Ag	Cd	Sn	Sb	Bi
Chalcopyrite	PN20-11											
	Min.	0.4		0.0	29	46	48	0.3	6.1	6.0	1.3	2.9
	Max.	21	**34.0**	10	30	129	92	101	20	8.9	89	2.9
	Mean (8)	7.6		2.1	29	62	67	20	9.8	7.1	24	2.9
	1σ	12		4.5	0.4	28	13	34	5.0	0.9	34	-

Bold values of Pb and Cu correspond to internal standards obtained using EPMA. * Samples with trace element concentrations determined by EPMA.

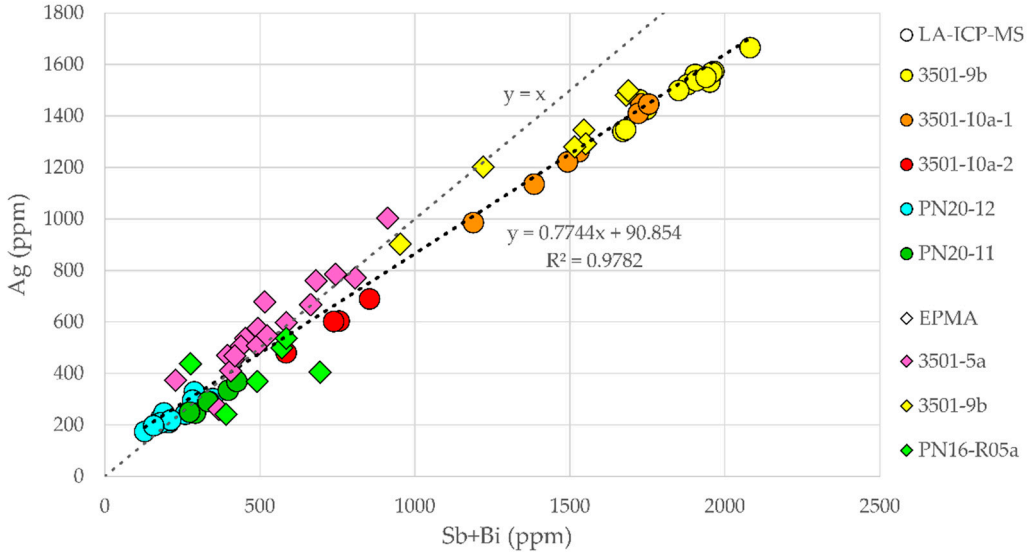

Figure 7. Ag versus Sb + Bi plot for trace elements in galena from MP samples (3501-10a-1 and 3501-10a-2 correspond, respectively, to galena from zone 1 and 2 on Figure 3b) and PN samples. Circles and diamonds represent LA-ICP-MS and EPMA analyses, respectively. The correlation line was drawn using all the dataset; the correlation coefficient is given by R^2.

The tetrahedrite group is a copper sulfosalt solid solution between tetrahedrite (Sb), tennantite (As), and freibergite (Ag) end-members [72,73]. The tetrahedrite group mineral is found as anhedral grains often in intergrowth with galena, chalcopyrite, phengite, and monazite (Figures 4 and 5). In both deposits, the tetrahedrite group displays mainly between the tetrahedrite (Sb) and tennantite (As) end-member (Table 1), with mainly a tennantite core and tetrahedrite rim observed in PN (Figure S1). In PN16-R05a, both galena and tetrahedrite show a poikilitic texture with inclusions of microquartz (Qz2), phengite, and florencite opposite to the inclusion-free texture (Figure 5a,d). The tetrahedrite grains display significant intragranular variations for Sb (21–25 wt%), As (3.2–5.6 wt%), and Ag (5.3–6.7 wt%). These variations reflect a complex zoning with a good correlation between Sb and Ag and an anticorrelation between As and Sb-Ag. Chemical zoning in tetrahedrite is not readily correlated with poikilitic or inclusion-free textures. However, tetrahedrite shows intergrowth texture with a Pb-Ag-depleted galena, which is in agreement with the tetrahedrite-preferred host for Ag-Sb in case of cocrystallizing tetrahedrite–galena assemblage [74].

Pyrite is ubiquitous in both Pb-Ag deposits and mainly found as (i) inclusions within galena or (ii) as the main ore mineral in sample 3501-5, where it forms a vein-type structure. Pyrite is usually found as subeuhedral to euhedral cubic crystals that may contain inclusions of galena, barite, phengite, hematite, florencite, and monazite. The inclusions may locally highlight a cubic growth zoning pattern (Figure 5e,f).

Chalcopyrite was only, but systematically, identified in the PN samples, associated with galena in millimetric veins perpendicular to the foliation, and in inclusions or intergrowth with the galena and tetrahedrite–tennantite aligned within the foliation (Figures 3c and 4e,f). All of the chalcopyrite trace elements contents are under 130 ppm, with no significant variation (Table 1). Other ore sulfides–sulfosalts, such as bournonite, cobaltite-gersdorffite, and sphalerite, were exceptionally observed in our samples.

7. Thermobarometric Results

7.1. Chlorites

Rosette-shape chlorite aggregates show an oscillatory zoning pattern in BSE images (Figure 8) and X-ray maps, mainly caused by Fe and Mg content variations (XMg = Mg/(Mg + Fe_{tot})). Based on variations in Mg, Si, Al, and Mn content, three different composition

zones can be recognized from the core to the rim of the rosette (Figure 8; Table 2). Three representative composition domains (Figure 8) were selected from the chlorite zoned map (n = 36,616). The chlorite zones have a size of 138, 86, and 66 pixels from Chl1 1 to Chl3, respectively. From core (Chl1) to the rim (Chl3), the Mg and Al increase, while Si, Fe, and Mn decrease with an Mg-poor, Fe-rich intermediate rim (Chl2) (Figure 8). The Si and Al anticorrelation do not follow exactly the same features as the XMg and Mn contents. The Si and Al contents have a moderate chemical transition occurring in the XMg-poor chlorite (Chl2). Textures and chemical zoning, from Chl1 to Chl3, display chlorite growth without dissolution patterns. Except for FeO and MgO contents, other chemical variations are under 1 wt% (Table 2). The Mn content displays an oscillatory zoning anticorrelated with the XMg zoning (Figure 8). It reaches its maximum with 0.065 apfu in the Chl2 domain. Assuming that the Fe measured is purely divalent, chlorite compositions are very close to the calculation limits of the semiempirical and thermodynamic models, with an average vacancy value of 0.03 ± 0.03 apfu (Masci, [75] and references therein). So, to avoid meaningless temperatures (e.g., negative or >1000 °C values using Inoue et al. [76] and Bourdelle et al. [77]), it was necessary to evaluate the $Xfe^{3+} = Fe^{3+}/Fe_{tot}$ value to approach the real chemical chlorite compositions and, by extension, to estimate the chlorite temperature formation. The Xfe^{3+} estimated with the chlorite–quartz–water multiequilibria approach of Vidal et al. [61] is 32 ± 5% for Chl1, 30 ± 4% for Chl2, and 27 ± 5% for the Chl3. Then, the ranges of temperature calculated for each zone are 285 ± 30 °C, 280 ± 30 °C, and 315 ± 35 °C, for Chl1, Chl2, and Chl3, respectively (Figure 8f).

Table 2. Representative EPMA chlorite and phengite compositions for the MP and PN ores. Standard deviations (σ) are expressed within parentheses. Oxides are expressed in wt% and elementary atoms per formula unit (apfu). Sum VI corresponds to the octahedral sum.

Samples														
					3501-5b (MP)								**PN16-R05a**	
Mineral	**Chl1**		**Chl2**		**Chl3**			**Ph1**		**Ph2**		**Ph**		
SiO_2	26.70	(0.60)	26.31	(0.54)	26.52	(0.66)		49.09	(1.11)	49.73	(0.72)	48.59	(1.13)
Al_2O_3	19.66	(0.31)	19.52	(0.33)	20.54	(0.31)		26.57	(0.52)	25.80	(0.47)	31.20	(0.72)
FeO	27.89	(0.49)	28.61	(0.56)	25.84	(0.61)		4.70	(0.40)	4.46	(0.30)	1.15	(0.10)
MgO	14.09	(0.29)	13.00	(0.21)	15.23	(0.55)		2.39	(0.11)	2.42	(0.08)	2.00	(0.13)
MnO	0.35	(0.10)	0.56	(0.08)	0.35	(0.08)		0.04	(0.06)	0.04	(0.01)	-	
K_2O	-		-		-			10.19	(0.22)	10.04	(0.21)	10.83	(0.20)
Na_2O	0.03	(0.01)	0.03	(0.01)	0.03	(0.01)		0.35	(0.22)	0.43	(0.18)	0.14	(0.06)
CaO	0.03	(0.02)	0.02	(0.02)	0.04	(0.03)		0.04	(0.06)	0.08	(0.08)	-	
TiO_2	0.01	(0.03)	0.01	(0.03)	0.04	(0.06)		0.02	(0.01)	0.02	(0.00)	0.14	(0.06)
Total	88.76	(0.84)	88.04	(0.82)	88.58	(1.08)		93.38	(1.19)	93.03	(0.74)	94.11	(1.21)
apfu			*(14 anhydrous oxygen basis)*							*(11 anhydrous oxygen basis)*			
Si	2.81	(0.04)	2.81	(0.04)	2.77	(0.04)		3.38	(0.04)	3.43	(0.03)	3.26	(0.04)
Al	2.44	(0.05)	2.46	(0.03)	2.53	(0.05)		2.16	(0.05)	2.10	(0.04)	2.47	(0.05)
Fe	2.46	(0.04)	2.56	(0.05)	2.26	(0.06)		0.27	(0.02)	0.26	(0.02)	0.06	(0.01)
Mg	2.21	(0.04)	2.07	(0.03)	2.37	(0.07)		0.25	(0.01)	0.25	(0.01)	0.20	(0.02)
Mn	0.03	(0.01)	0.05	(0.01)	0.03	(0.01)		-		-		-	
K	-		-		-			0.90	(0.02)	0.88	(0.02)	0.93	(0.02)
Na	-		-		-			0.05	(0.03)	0.06	(0.02)	0.02	(0.01)
Ca	-		-		-			-		0.01	(0.01)	-	
Ti	-		-		-			-		-		0.01	(0.00)
∑VI	5.97	(0.03)	5.96	(0.03)	5.97	(0.03)	Xcel	0.40	(0.04)	0.43	(0.02)	0.25	(0.02)
XMg	0.47	(0.01)	0.45	(0.01)	0.51	(0.01)	XMs	0.50	(0.04)	0.47	(0.03)	0.68	(0.03)
Xfe^{3+}	32	(5)	30	(4)	27	(5)	XPrl	0.05	(0.03)	0.05	(0.02)	0.05	(0.03)
T (°C) *	285	(30)	280	(30)	315	(35)	XPg	0.04	(0.02)	0.05	(0.02)	0.02	(0.01)

* Vidal et al. [40,41]; Pinit = 5 kbar.

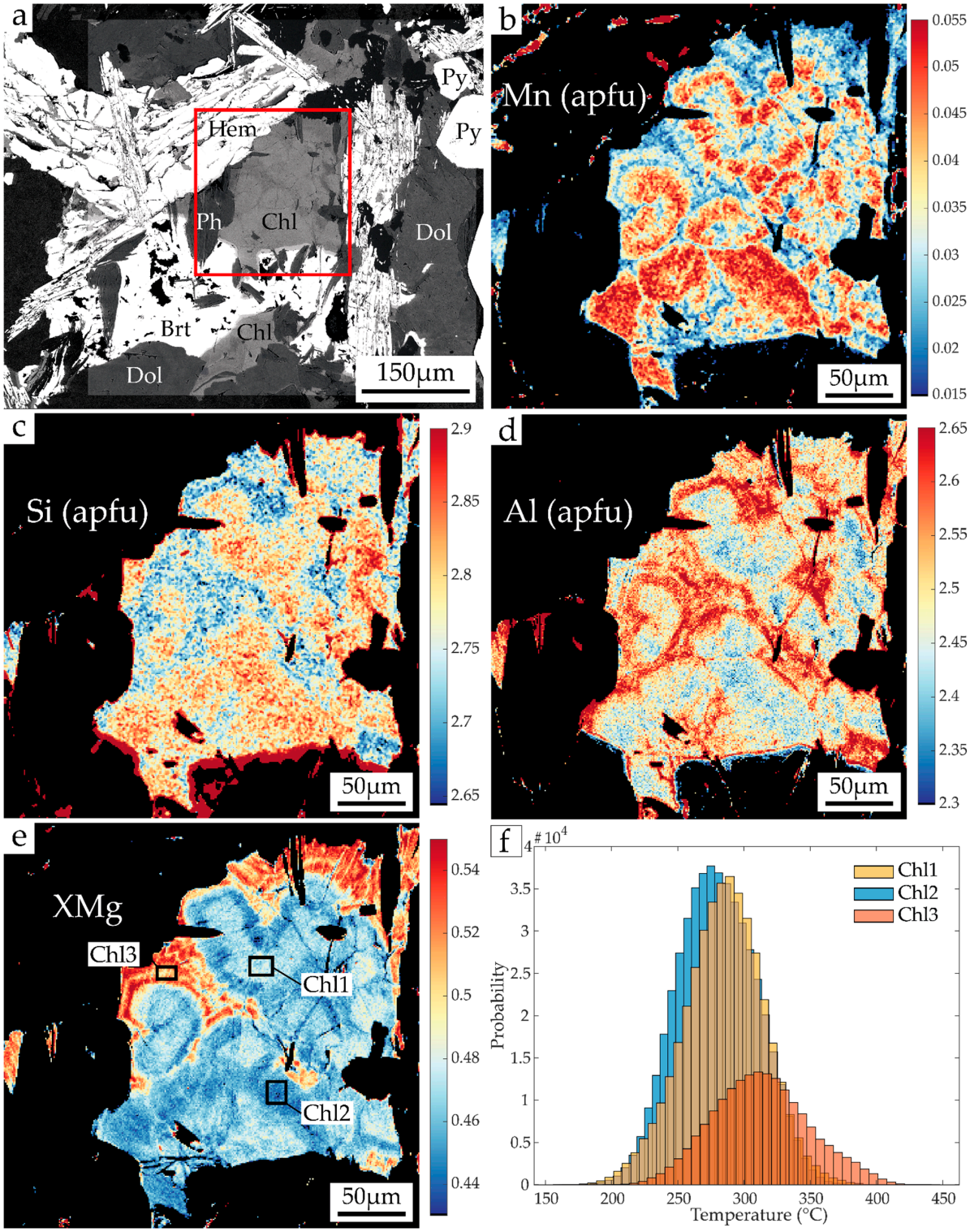

Figure 8. (**a**) Backscatter (BSE) electron image of euhedral rosette-shape chlorite aggregates with chemical zoning. The red frame displays the zone of the X-ray map. Quantified X-ray chlorite maps (in apfu) of: (**b**) Mn; (**c**) Si; (**d**) Al; (**e**) XMg content (XMg = Mg/(Mg + Fe_{tot})) with black boxes showing the pixel zone analyzed of each representative chlorite zone, as discussed in the text. (**f**) Histogram of chlorite temperature formation calculated on each pixel from the map.

The empirical thermometer of Cathelineau [64] based on the Al^{IV} content shows a lower temperature range for Chl1 and Chl2 (320 ± 10 °C) than for Chl3 (330 ± 10 °C). Thus, the Al^{IV} content is similar for Chl1 and Chl2 (1.19 ± 0.03 apfu) and slightly higher for Chl3

(1.23 ± 0.03 apfu). Chl1 and Chl2 display a similar Al^{IV} content (1.19 ± 0.03 apfu), while Chl3 shows slightly higher Al^{IV} content (1.23 ± 0.03 apfu). The range (280–330 °C) and the tendency of increasing temperature between Chl1–Chl2 and Chl3 are similarly displayed by both empirical and thermodynamic chlorite thermometers.

7.2. Phengites

In the chlorite-bearing sample (3501-5b), euhedral acicular phengite is commonly found parallel and in contact with the individual platelet Chl3 crystals (Figure 8a) and is thus assumed to be cogenetic with Chl3, at least for its outer compositions. Variations in Si and Al contents allow two groups of phengite to be distinguished (Table 2; Figure 9a,b). The first group (Ph1: n = 212) has lower Si and higher Al contents (3.31–3.45 and 2.06–2.24 apfu, respectively) than the second group (Ph2: n = 120, Si of 3.37–3.52 apfu, Al of 2.00–2.18 apfu). The temperature of Ph1 growth estimated with the thermometer of Dubacq et al. [59] is slightly higher (275–360 °C at a fixed reference pressure of 5 kbar) than that for Ph2 (250–330 °C, Figure 9). However, the quantitative point analyses (used as internal standards for the Ph map) show intermediate temperature included within both Ph zones (individual Ph from MP: n = 18, 275–310 °C at 5 kbar, Figure 9). The Ph1 and Ph2 P-T dispersion may be explained by the Ph textures (acicular or larger crystals) and are not sustained by the individual Ph analyses from the same area. Thus, for more accuracy and representativeness, the individual Ph data were used to constrain the P-T deposit formation. Following the approach proposed by Lanari et al. [29], approximative pressure conditions for the growth of phengite and chlorite aggregates are obtained by combining results of phengite–quartz–water (for Individual Ph from MP) and chlorite–quartz–water (for Chl3) models, respectively. They yield at 315 ± 35 °C and 6.25 ± 0.75 kbar (Figure 9).

The PN phengite shows no significant variations between microstructural sites, and overall mineralogical variations are moderate (n = 15, Table 2), with Si content ranging from 3.19 to 3.39 apfu. The PN phengite displays Al content ranging between 2.32 and 2.55 apfu and Fe content between 0.05 and 0.07 apfu. Despite the PN analyses of phengite being in the same SiO_2 content range as those from MP, it appears that PN phengite is closer to the muscovite + paragonite end-members (0.70 ± 0.04) in comparison to those from MP (0.54 ± 0.02). From both deposits, the maximum pyrophillitic ratio calculated in a single analysis is 0.10 (XPrl in Table 2). Hence, the Si content is controlled by the Tschermark substitution between celadonite and muscovite (respectively, XCel and XMs, as shown in Table 2) at the same bulk rock composition (Dubacq et al. [59] and references therein). However, at a fixed pressure (5 kbar), the PN phengite growth temperature using Dubacq et al. [59] ranges between 280 and 330 °C, which is in agreement with both the MP phengite and chlorite temperature formation (Figures 8 and 9).

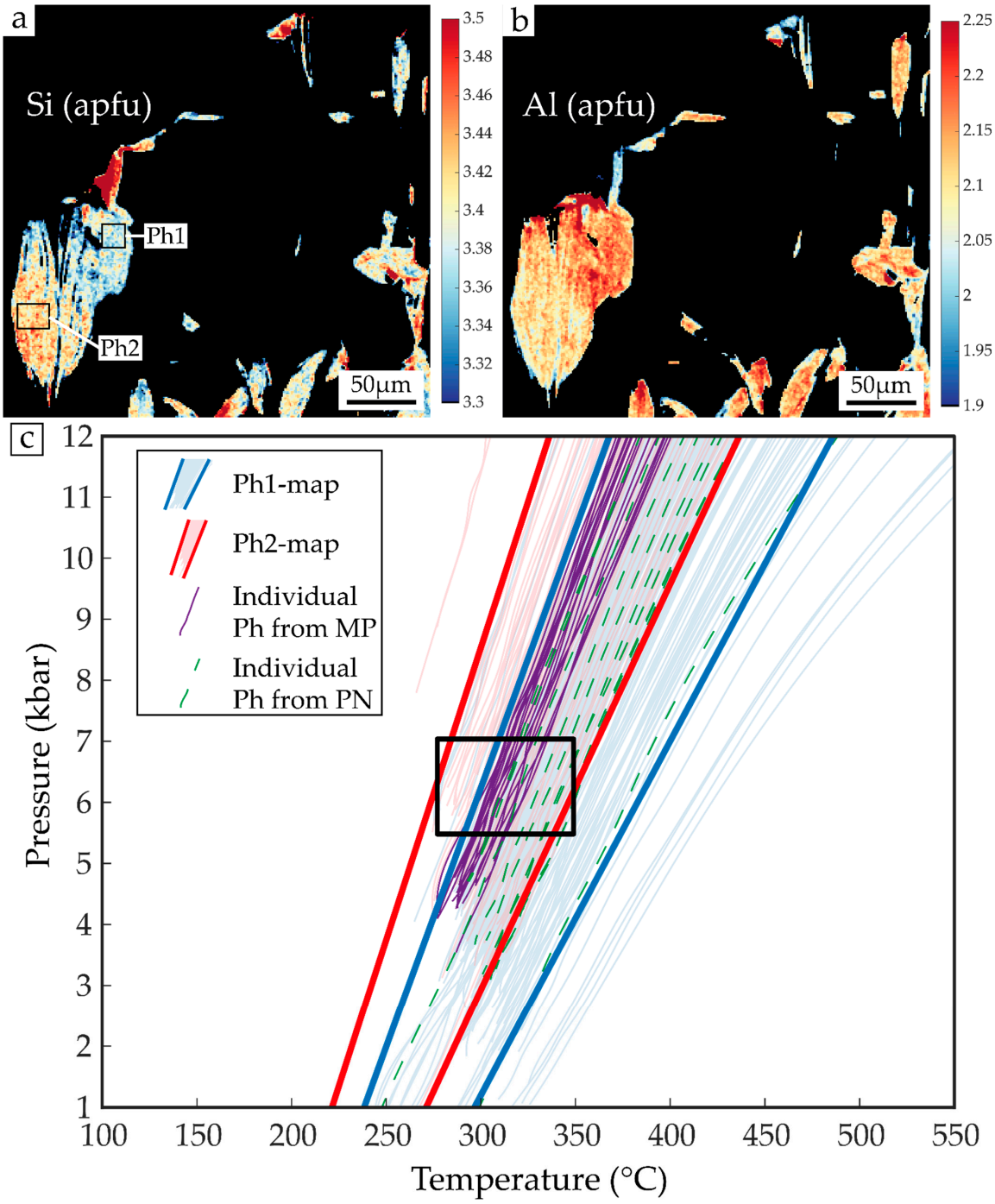

Figure 9. (**a**,**b**) Quantified X-ray phengite maps (in apfu) of the Si content (**a**) and the Al content (**b**). The black boxes show the pixel zones analyzed. (**c**) Phengite P-T estimates (lines) using the method of Dubacq et al. [59]. The box is constructed using the result of Chl3 thermometry (Figure 8f) and the punctual data. For a given temperature, pressure has been estimated using the phengite P-T equilibrium lines of the punctual data from the map area. Boundaries of the Ph1 and Ph2 were determined using more than 95% of P-T lines for each zone.

8. Monazite Characterization and U-Pb In Situ Dating

Despite the micrometric size (<10 µm) and similarity in contrast and brightness between the monazite and barite in the SEM-BSE mode (Figure 5e), few crystals of monazite were found in all rock samples, except for the massive sulfides. However, in only one sample from the PN deposit (PN16-R05a), monazite was abundant and large enough for

detailed petrological characterization and further chemical and isotopic dating. For the MP deposit, monazite grains from three different samples were dated.

8.1. Monazite Characterization and Composition

In PN16-R05a, monazite crystals show an elongated subhedral shape with a length and width up to 100 µm and 20 µm. Monazite has a poikilitic texture with inclusions of quartz, phengite, and florencite. It occurs in the recrystallized Qz2 domain or inclusions in sulfide–sulfosalt. Elongated grains can share sharp straight boundary contact with sulfide–sulfosalt or phengite. In PN16-R05a, the monazite grains are zoned (Figure 10; Supplementary Table S3). The core corresponds to Nd–monazite (Nd > Ce wt% content) enriched in middle-REE, especially in Eu (up to 5 wt%), U, Th, Ca, Si, and Y. The rim corresponds to a Ce–monazite rim (Ce > Nd content, Th < 3 wt% and Ca < 0.8 wt%) enriched in La (light-REE). In the MP samples, monazite shows minor variations with a typical composition of monazite–(Ce) and a lower U and Th compared to those obtained in the core of the PN monazite–(Nd).

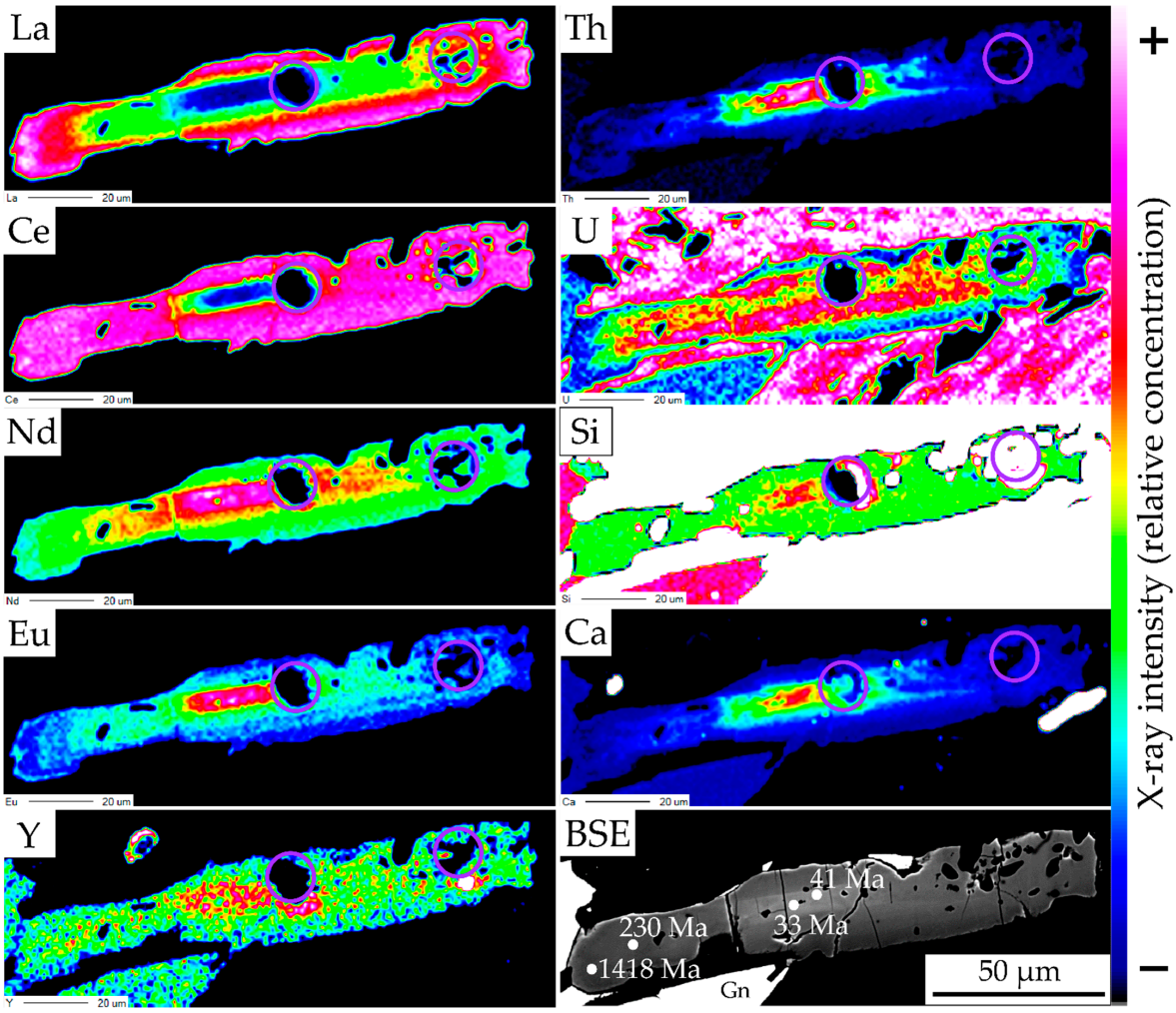

Figure 10. Elementary maps (La, Th, Ce, U, Nd, Si, Eu, Ca, Y) of a Peisey-Nancroix monazite surrounded by galena (white) and quartz (black; PN16-R05a), performed using electron microprobe and BSE image showing electron microprobe ages (white dots). The violet circles show LA-ICP-MS spots of U-Th-Pb dating.

8.2. Monazite U-Th-Pb Chemical Dating

In PN16-R05a, U can reach up to 1.24 wt% in the core of monazite–(Nd). Uranium generally tends to decrease towards the rim. Similarly, Th is high but decreases to extremely

low values towards the rim. In the Th- and U-rich core, it was possible to calculate a chemical U-Th-Pb age as young as 33 Ma (Figure 10), excluding the presence of an inherited core. The rim provides meaningless older ages and is to low contribution of radiogenic Pb in the U- and Th-poor rim (EPMA ages of Figure 10).

As regards MP monazite grains, the systematically low Pb content, below or close to the detection limit (Supplementary Table S3), could not allow calculating an age, but also suggests a young crystallization with no evidence of an older event.

8.3. Monazite In Situ Isotopic U-Pb Dating

In total, 44 LA-ICP-MS analyses were performed on twenty-six monazite individual grains on PN16-R05a (PN ore), and seventeen analyses were performed on fourteen monazite grains from three MP samples (3501-4b, n = 3; 3501-5b, n = 11; 3501-10a, n = 3), as shown in Table 3.

Table 3. Summary of the LA-ICP-MS raw data for Peisey-Nancroix (PN16-R05a) and Macôt-la Plagne monazite (3501-4b, 3501-5b, and 3501-10a). Note that monazite grains are referenced by the first digit in the analysis n° after the sample names, and the spot numbers in each monazite grain are displayed by the third and last digit.

Analysis n°	Measured Ratio				Analysis n°	Measured Ratio			
	$^{207}Pb/^{206}Pb$	±(1σ)	$^{238}U/^{206}Pb$	±(1σ)		$^{207}Pb/^{206}Pb$	±(1σ)	$^{238}U/^{206}Pb$	±(1σ)
PN16-R05a-1 *	0.813	0.016	8.168	0.123	PN16-R05a-6-2	0.133	0.012	140.6	4.154
PN16-R05a-1-2 *	0.726	0.018	29.43	0.520	PN16-R05a-15-1	0.101	0.008	170.6	4.368
PN16-R05a-2 *	0.360	0.014	107.5	2.312	PN16-R05a-15-2	0.208	0.015	145.6	4.238
PN16-R05a-3-1 *	0.695	0.033	23.16	0.735	PN16-R05a-17-1	0.268	0.015	120.3	3.041
PN16-R05a-4 *	0.665	0.033	43.35	1.390	PN16-R05a-17-2	0.236	0.013	145.8	3.612
PN16-R05a-6-1 *	0.125	0.006	162.9	2.918	PN16-R05a-18-1	0.825	0.024	4.212	0.053
PN16-R05a-22-1 *	0.077	0.005	170.1	3.471	PN16-R05a-23-1	0.420	0.021	106.6	2.728
PN16-R05a-22-2 *	0.111	0.007	159.5	3.561	PN16-R05a-23-2	0.856	0.027	1.035	0.014
PN16-R05a-11-1 *	0.619	0.013	47.19	0.646	PN16-R05a-24-1	0.845	0.028	2.736	0.037
PN16-R05a-11-2 *	0.425	0.015	93.98	1.943	PN16-R05a-7-1	0.378	0.020	105.2	2.764
PN16-R05a-10-1 *	0.171	0.006	157.0	2.711	PN16-R05a-25-1	0.482	0.025	88.65	2.358
PN16-R05a-10-2 *	0.229	0.012	137.0	3.378	PN16-R05a-16-1	0.154	0.017	167.2	6.432
PN16-R05a-12-1 *	0.117	0.005	188.3	3.192	PN16-R05a-21-2	0.332	0.025	135.5	4.957
PN16-R05a-12-2 *	0.227	0.007	145.1	2.317	3501-5b-13-1	0.799	0.043	8.834	0.310
PN16-R05a-12-3 *	0.213	0.008	137.0	2.439	3501-5b-16-1	0.703	0.045	21.53	0.867
PN16-R05a-12-4 *	0.297	0.012	123.3	2.433	3501-5b-16-2	0.791	0.068	9.173	0.537
PN16-R05a-14-1 *	0.226	0.010	139.7	2.731	3501-5b-17-1	0.586	0.037	55.01	2.057
PN16-R05a-14-2 *	0.216	0.010	154.6	3.344	3501-5b-24-1	0.231	0.030	137.2	7.150
PN16-R05a-8-1 *	0.325	0.012	129.0	2.497	3501-5b-28-1	0.644	0.101	20.73	2.068
PN16-R05a-8-2 *	0.274	0.009	136.8	2.433	3501-5b-30-1	0.509	0.043	78.06	3.656
PN16-R05a-8-3 *	0.260	0.009	129.4	2.343	3501-5b-37-1	0.539	0.046	79.74	3.879
PN16-R05a-13-1 *	0.087	0.003	211.4	3.129	3501-5b-42-1	0.499	0.033	89.21	3.183
PN16-R05a-13-2 *	0.251	0.012	133.9	3.047	3501-5b-53-1	0.503	0.065	84.75	6.176
PN16-R05a-19-1 *	0.094	0.005	173.0	3.293	3501-5b-54-1	0.482	0.043	115.5	5.600
PN16-R05a-19-2 *	0.087	0.006	179.2	4.175	3501-4b-1-1	0.501	0.035	65.75	2.550
PN16-R05a-5-1 *	0.647	0.024	50	1.150	3501-4b-1-2	0.475	0.029	83.26	2.704
PN16-R05a-9-1 *	0.189	0.007	174.5	3.046	3501-4b-2-1	0.600	0.028	59.99	1.403
PN16-R05a-9-2 *	0.219	0.008	153.1	2.580	3501-10a-13-2	0.802	0.044	11.90	0.438
PN16-R05a-20-1 *	0.220	0.010	143.1	3.070	3501-10a-12-1	0.859	0.032	7.130	0.177
PN16-R05a-20-2 *	0.194	0.009	155.5	3.386	3501-10a-12-2	0.878	0.028	1.638	0.037
PN16-R05a-21-1 *	0.192	0.007	142.2	2.428					

* 15 µm spot size; 10 µm spot size to all other.

In the Tera–Wasserburg diagram, the data align well on a single line for both deposits. The lower intercept of the Concordia line provides an estimated age (without correction) of 35.1 ± 0.6 Ma (MSWD = 2.1; n = 38) for PN (Figure 11a) and 34.2 ± 3.5 Ma (MSWD = 1.3; n = 17) for MP (Figure 11c). By fixing the value of the initial $^{207}Pb/^{206}Pb$ ratio at 0.835, using the bulk-Pb evolution model of Stacey and Kramers [78] and Cumming and Richards [79], it is possible to correct the calculated age from the common Pb contamination. Thus, the corrected age is 34.9 ± 0.5 Ma (MSWD = 2.1, n = 38/44) for PN monazite grains (Figure 11b) and 33.1 ± 2.9 Ma (MSWD = 1.3, n = 17) for MP (Figure 11d). Anchoring the Pb initial

composition to the common Pb values (Stacey and Kramers model [78]) has no significant impact on the monazite age, indicating that the isotopic Pb composition of the MP and PN mineralizing fluids are close to the predicted common Pb values, opposite to some mineralizing fluids in relation with the Penninic front [80,81]. Moreover, even if monazite grains from three different rock samples are considered for the MP deposit, there is one sample (3501-5b) more represented and well dispersed along the Discordia line, which gives an age of 32.15 ± 3.25 Ma (n = 11) within the uncertainty of the age obtained by considering the entire MP dataset (Figure 11d).

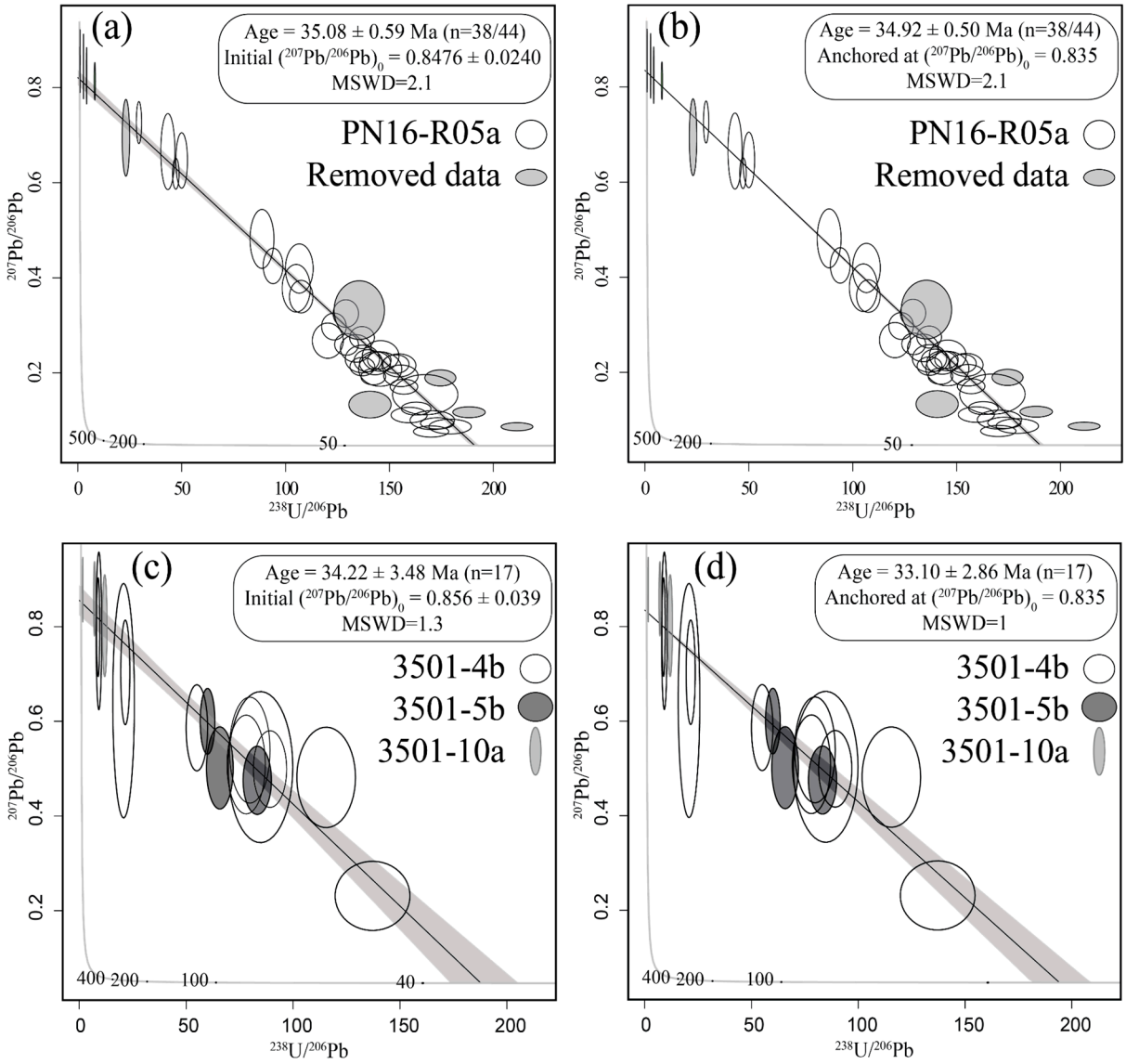

Figure 11. Tera–Wasserburg diagrams of the monazite LA-ICP-MS analysis (Table 3) for the Peisey-Nancroix (**a**,**b**) and the Macôt-la Plagne (**c**,**d**) deposits. (**a**,**c**) provides Discordia lines and ages calculated without any correction, whereas for (**b**,**d**) the initial $^{207}Pb/^{206}Pb$ ratio is fixed at 0.835, using the bulk-Pb evolution model of Stacey and Kramers [78] and Cumming and Richards [79], to correct the calculated age from the common Pb contamination. Forty-four analyses from twenty-six monazite grains (white ellipses in (**a**,**b**)) were used for calculating the age of PN16-R05a (gray ellipses (n = 6) were removed from the age calculation after SEM control, Section 4.4). Seventeen analyses from fourteen monazite grains were used for calculating the age (without removed data) from the Macôt-la Plagne samples.

9. Discussion

The Pb-Ag mineralizations of the two MP and PN deposits are located in a similar litho-structural domain. Further, they show a main similar mineral paragenesis, deformation microstructure, and ages, suggesting that they formed under similar conditions. Amongst the mineralogical variations detected, we can notice: (i) between deposits, chalcopyrite exclusively occurs within PN; (ii) through the MP deposit (Figure 1c); higher amounts of barite are found within the Sarrazins-type veins contrary to the pod-type ores; (iii) depending on the sample, a high variability of the monazite distribution. Despite these paragenesis variations, the microstructural, thermobarometric, and geochronological similarities between the two deposits is legitimate, and the metallogenic model behind the PN and MP deposits will be further discussed indistinctly.

9.1. An Alpine Pb-Ag Mineralization

A main issue for determining metallogenic models of ore deposits located in orogenic belts resides in the possibility of inheritance or remobilization through time from the initial crystallization/deposition up to the different orogenic deformation stages (e.g., [82–85]). In this study, major efforts were thus made to investigate mineral microstructures and compositional variations for discriminating crystallization steps. Whatever the disseminated or massive texture of the Pb-Ag mineralization, the mineral parageneses are very similar in all investigated samples. They display intergrown microstructures, suggesting cogenetic growth during a single hydrothermal event (Figures 4f and 5). However, mineral textures are often not sufficient to correlate or decouple mineralization phases and/or fluid evolution during crystal growth between ore samples, especially without controlling the in situ structural context of the investigated samples within the deposit. Trace elements associated with precise textural observations are a powerful method to constrain the number of crystallization phases and/or fluid evolution in a mineralization stage. Galena is the only sulfide to occur in all rock samples. Galena is quite homogeneous in trace elements, except for Ag and Sb. Fine-grained galena disseminated between intergranular gangue grains or in vein-type was depleted in Ag-Sb compared to the massive galena. Intragranular zoning was observed in sulfide (pyrite), sulfosalt (tetrahedrite), silicates (chlorite and phengite, Figures 8 and 9), carbonates (dolomite–ankerite group, Figure 8a), and accessory minerals (monazite, Figure 10). Whatever the minerals and their textures, the inclusions are very similar: they are generally represented by phengite and quartz, which commonly formed during the Alpine tectonics within the External Briançonnais domain [29,31]. More exceptional is the presence of microspheric inclusions of florencite in sample PN16-R05a. This unique feature may be due to higher and uncommon REE composition (see Supplementary Table S3) combined with the low-grade metamorphic conditions [86]. In this PN sample, ubiquitous florencite microinclusions in recrystallized isometric and isogranular Qz2 (Figure 5c), sulfides (galena, Figure 5b), sulfosalt (tetrahedrite, Figure 5b), and monazite (Figure 5b) associated with intergrown microstructures suggest that the mineral paragenesis occurred during a single crystallization stage at relatively low-grade metamorphic conditions. Mineral zoning is thus suggested to result from the physico-chemical evolution (P, T, speciation) of the fluid through time during the crystallization.

A single-stage crystallization during the Alpine orogeny is independently confirmed by monazite in situ dating. In this study, monazite is interpreted to be cogenetic of the ore mineralization based on their syngenetic texture with sulfides–sulfosalts: (i) monazite is included within galena and pyrite (Figure 5); (ii) it is intergrown with galena and tetrahedrite (Figure 5a,b); (iii) it can have a poikilitic texture and it contains the same inclusions (quartz, phengite, florencite; Figure 5a,b) as the sulfide–sulfosalts. Their elongated shape with fractionation of LREE/HREE from core to the rim is a relatively common feature of low-grade metamorphic monazite ($T < 400$ °C; [87–90]). Monazite zoning is thus attributed to different stages of formation [88] or evolution in pore fluid chemistry from early diagenesis to very low-grade metamorphism [91]. Prior to isotopic dating, preliminary EPMA U-Th-Pb dating at microscale excludes pre-Alpine ages in monazite. In the MREE-

and Eu-rich core of monazite–(Nd), the exceptionally high U (and Th) contents were high enough that Pb can be detected to determine an age around 33 Ma (Figure 10). For other compositions, radiogenic Pb was, however, insufficient, and common Pb too abundant for EPMA dating. The EPMA Alpine age was thus sharpened using in situ LA-ICP-MS dating, providing an age of about 35 Ma. Data are more accurate for the PN sample than for the MP samples, with a good alignment of the entire U-Pb dataset on the Tera–Wasserburg diagram, which intersects the concordia at 35.1 Ma ± 0.6 Ma. This indicates that the age of the different monazite zoning could not be distinguished using LA-ICP-MS, and that mineralization probably occurred during a time interval below the analytical uncertainties obtained from the calculated age (0.6 Ma). Based on the paragenetic sequence, this age and duration are thus assumed to be valid for the overall Pb-Ag mineralization.

Historically, textural variations in the Triassic quartzite are interpreted either as a depositional facies' variation during sedimentary deposition [3,4] or as a tectonic crushing [6,7]. These two views have sparked the debate between two main metallogenic models for PN and MP deposits with either: a syn-diagenetic origin [3–5,13] or a tectonic cause associated with the Alpine collision [6,7,30,31]. Yet, a sedimentary/diagenetic origin can definitely be excluded based on the mineral, thermobarometry, and geochronology datasets. Such epigenetic models at relatively similar thermobarometric conditions are coherent with some recent reappreciations of other worldwide Pb-Zn(-Ag-Cu-Fe) deposits from Australian and Chinese belts [14,18].

9.2. A Mineralizing Fluid Circulation during the D1 Deformation Stage

Field observations combined with quartz and sulfides microstructures allow reconciling the apparent stratiform texture with an ore mineralization occurring during the Alpine ductile deformation. All investigated samples show intense quartz recrystallization, up to quartzite mylonitization, in samples showing disseminated textures (Figures 3c and 4a,c,d). In a single thin section (PN20-11a; Figure 4), relics of initial Qz1 porphyroclasts are unevenly preserved from recrystallization. The progressive evolution of quartz recrystallization in association with mineralization migration is schematized in Figure 12. From step 1 to step 3, the Qz1 porphyroclasts show different degrees of recrystallization by newly formed isometric and equigranular microquartz (Qz2). In the first step, Qz1 porphyroclasts are well preserved with abundant cracks generated by high-stress conditions in the presence of the mineralizing fluids, as attested by the presence of galena within the sealed cracks (Figure 4b). More generally, Qz1 recrystallization into Qz2 is mainly restricted to cracks and pressure shadows. At step 1, the sulfide–sulfosalts are mainly observed in the foliation, at porphyroclasts' grain boundaries, or associated with Qz2 micrograins in dilation zones, sealed cracks, and strain shadows. This attests to the migration of the mineralizing fluids in the foliation, at grain boundaries, and within the porosity generated by fracturing or further dissolution [92]. Then, the (re)crystallization and mineralization propagate pervasively through the porphyroclast (step 2) up to reaching a complete porphyroclast recrystallization with no evidence of the initial Qz1 left (step 3). Concomitant Qz1 recrystallization with fluid propagation is underlined by the increasing sulfide and Qz2 proportion from steps 1 to 3. Truncated and elongated porphyroclast relics along the main foliation provide evidence of the action of the pressure solution in quartz deformation (S1) [93]. The presence of white mica aligned parallel to the foliation may play the role of a coating and retard the pressure solution (step 1) (Renard et al. [94] and references therein), thus favoring porphyroclast preservation (Figure 4a).

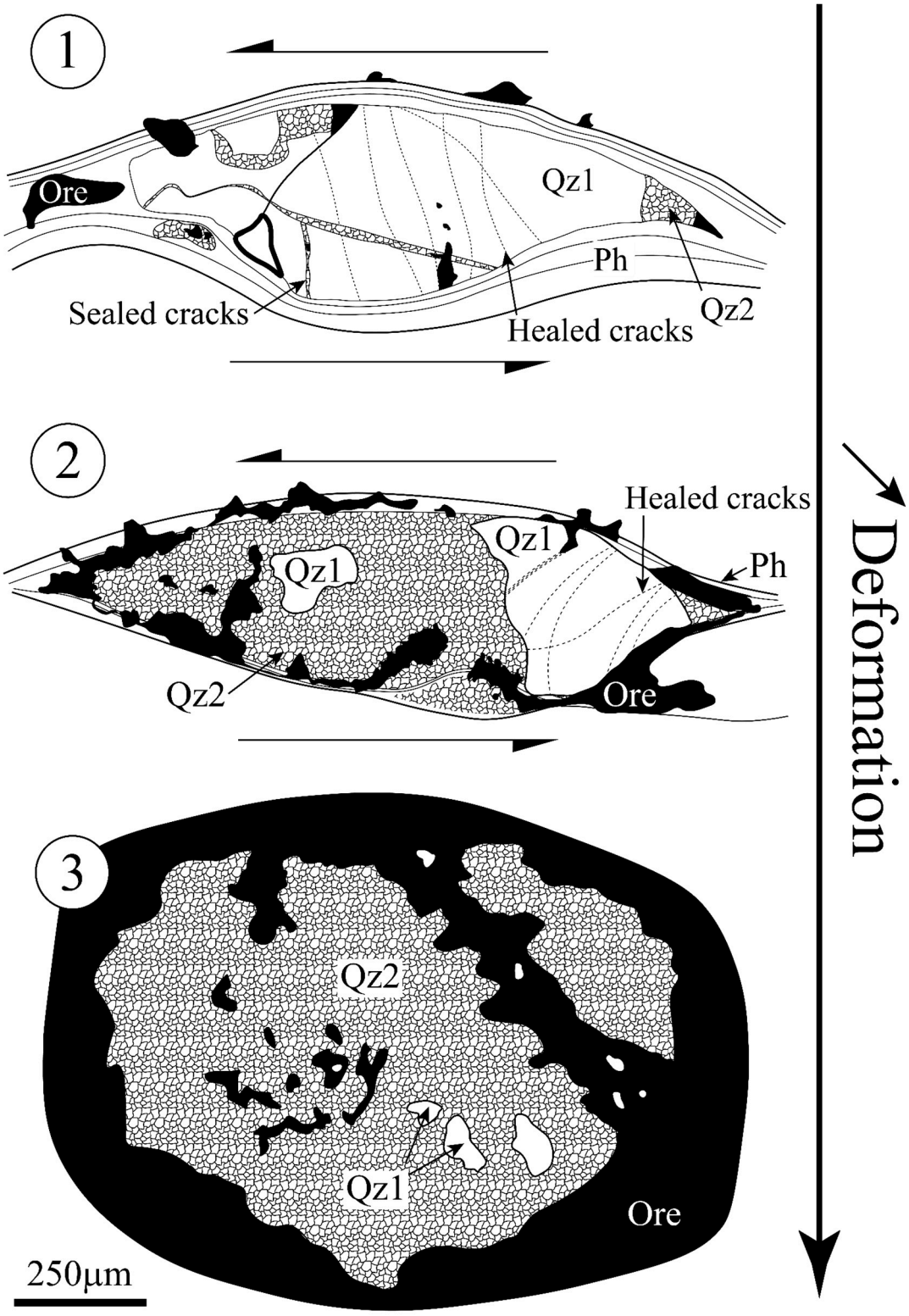

Figure 12. Scheme of quartz porphyroclast (Qz1) and textural evolution of the ore in mylonites due to increasing deformation (Step 1 to 3) and fluid circulation: from disseminated ore (step 1 and 2) to massive ore (step 3).

Fluid-assisted deformation is thus proposed as the main mechanism accounting for the initial fracturing and later porphyroclast recrystallization associated with sulfide precipitation following a scenario such as:

(i) a stress increase, probably due to seismic pumping up to reaching hydraulic fracturing [95,96], which is illustrated by the abundance of cracks in the porphyroclast and the vein-type texture of the samples;

(ii) a stress drop during fluid migration through the cracks, grain boundaries, and porosity generated by quartz dissolution–reprecipitation reactions [97]. Lower stress conditions are attested by the isometric and equigranular microstructure of the newly formed Qz2 grains and the euhedral shape of the mineralization (Figures 4 and 5c). It is in that stage that the sulfides–sulfosalts mineralization formed, through progressive precipitation from the mineralizing fluids propagating in the dynamically generated porosity.

Preferential orientation of the sulfides along the main foliation of the mylonite results from a syn-deformation ore genesis model associated with the Alpine collision.

9.3. P-T-t-d Correlation between the Genesis of the Pb-Ag Deposits and the Tectonics of the Briançonnais Zone

The Mine Fault (Figure 2) mylonitizes the Permian phyllitic quartzite and sericitoschist with top-to-the-NW deformation highlighted by deformed quartz porphyroclasts along the S1 foliation and the C′-type shear bands. In our mineralized samples, the mylonitic fabrics with deflection of the S1 foliations around the porphyroclast Qz1 relics is consistent with the mylonitic fabrics of nonmineralized phyllitic quartzite. Based on the similarities of the microstructures, we propose that the Pb-Ag mineralizations occur during the top-to-the-NW D1 deformation in the External Briançonnais [33].

This study constrains the main P-T-t-d conditions for ore genesis in PN and MP with an onset at 280 °C and a main stage of mineralization at 315 ± 35 °C, 6.25 ± 0.75 kbar and 35 ± 1 Ma. The P-T conditions are consistent with the Alpine peak metamorphic conditions recorded in the Briançonnais Houiller Zone (275 °C and 5.9 kbar) [29] and with the D1-D2 transition estimation for the cover of the Internal Briançonnais (Modane-Aussois units) and the "Nappe des Gypses" (350 °C and 6.5 kbar) [25,34]. These Alpine peak metamorphic conditions are estimated in the External Briançonnais between 34-35 MaMa by the D1-D2 transition recorded within the Modane-Aussois unit (Internal Briançonnais) [34], during the exhumation of the Internal Briançonnais on top of the External Briançonnais through NW-directed thrusting (Figure 13). These new P-T-t-d constraints suggest that the ore formed probably due to mineralized fluids flowing along the contact between the "Nappe des Gypses" and the Permo-Triassic sediments of the External Briançonnais (Figure 13). Thus, in light of the new ore formation model, we propose that the foliation that is parallel to the Internal Briançonnais Front, which is highlighted by the contact with the "Nappe des Gypses" in MP (noted S3 on Figure 1c), must be a S1 foliation reoriented by the thrusting of the "Nappe des Gypses" on top of the External Briançonnais. The important ore concentration in both deposits illustrated by the Pb and Ag production involves an important amount of fluid. A large part of the fluid source may come from the "Nappe des Gypses". Barré et al. [25] (and references therein) indicate that the gypsum dehydration into anhydrite, probably at the end of the prograde path, might release an amount of water estimated at 37%.

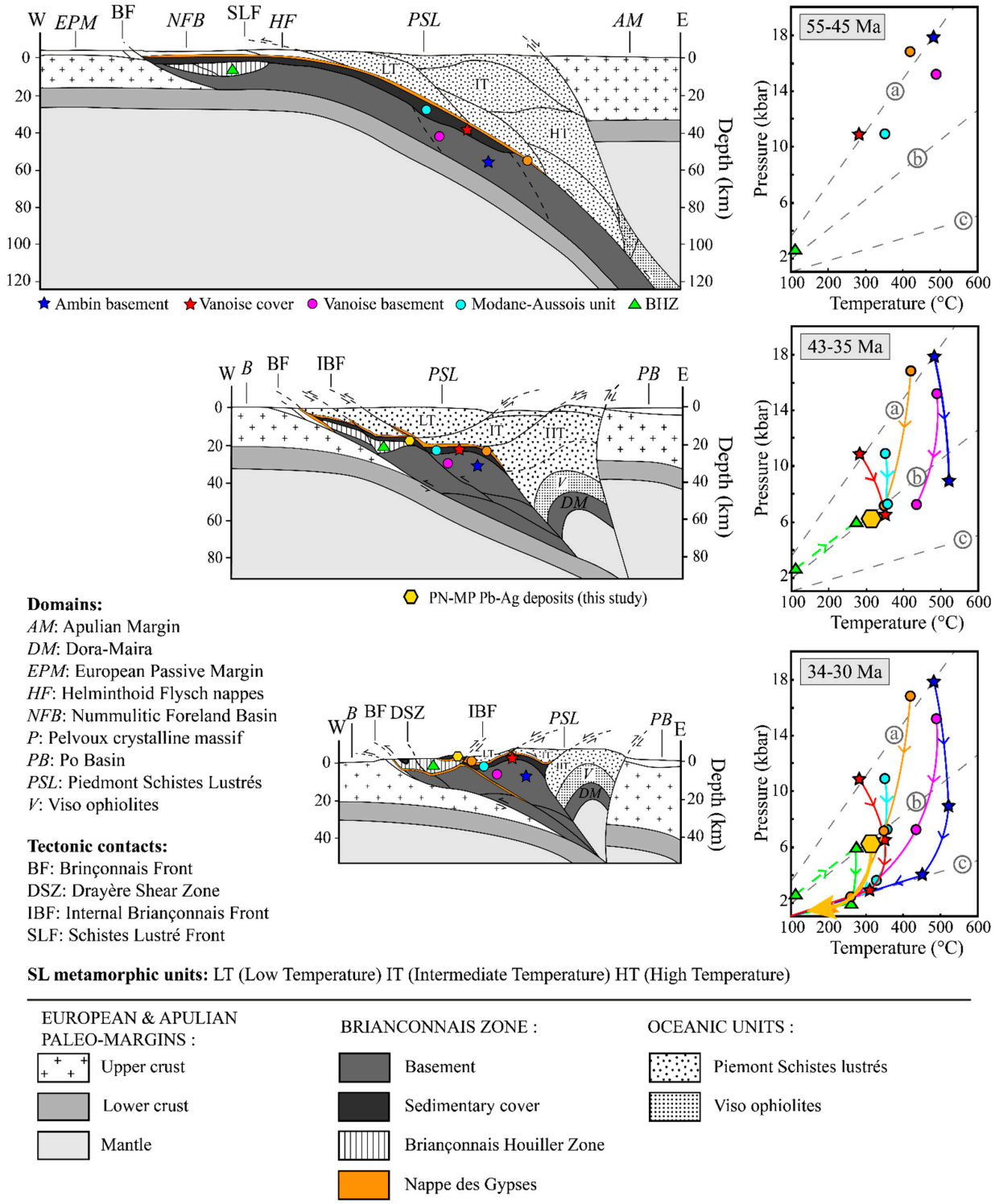

Figure 13. Possible kinematic reconstruction of this part of the Western Alps from Eocene to Oligocene modified after Lanari et al. [29] with associated P-T paths for Ambin basement and Vanoise cover [36], Vanoise basement, and Modane-Aussois units [34], "Nappe des Gypses" [25] Briançonnais Houiller Zone [29], and the PN-MP Pb-Ag deposits (this study). Geothermal gradients of 8 °C/km (a), 15 °C/km (b), and 40 °C/km (c) are also shown.

10. Conclusions

This integrative study shows how the complementary use of structural geology, petrology, trace element analyses in sulfides, chlorite–phengite thermobarometry, and in

situ U-Pb monazite dating was successful in constraining the P-T-t-d conditions of the fluid circulation responsible for Pb-Ag deposits located in a complex and polyphase orogenic history (the Peisey-Nancroix and the Macôt-la Plagne deposits). The main conclusions are:

1. Both Pb-Ag deposits are found in the same litho-structural context and show comparable paragenetic sequences attributed to a single mineralization episode with possible chemico-physical conditions evolution through progressive crystallization.
2. Despite the high Pb contents, the two Pb-Ag deposits could be successfully dated using the in situ LA-ICP-MS isotopic U-Pb dating of monazite. The geochronological dataset reveals that Pb-Ag mineralization formed during the Alpine orogenesis at about 35 Ma. P-T conditions of the mineralization are estimated at 315 ± 35 °C and 6.25 ± 0.75 kbar. These correspond to the Alpine peak metamorphism of the External Briançonnais.
3. P-T-t-d conditions, structural, and textural observation of deformed quartz porphyroclasts demonstrate a syn-kinematic Pb-Ag mineralization with the Alpine late-D1 deformation in the Internal Alps.

To our knowledge, this is the first time that an Alpine age is unambiguously proven for Pb-Ag deposits of the Western Alps. This methodology could be further applied to other low-grade metamorphic deposits from the Alps or other orogenic belts. In particular, understanding the transfer and source of the fluid, as here probably in association with the thrusting of the "Nappe des Gypses", will be of great interest to better characterize polymetallic mineralization during ductile deformation.

Supplementary Materials: The following supporting information can be downloaded at: https://www.mdpi.com/article/10.3390/geosciences12090331/s1, Figure S1: BSE image of a tennantite core-tetrahedrite rim inclusions within galena. Table S1. Mineralogical summary for the PN-MP deposits samples; Table S2. Resume of the U-Th-Pb monazite analysis conditions using LA-ICP-MS; Table S3. Summary of chemical EPMA analysis on monazite.

Author Contributions: M.B., M.R., I.D.-A. conducted fieldwork, performed sampling and samples preparation; M.B., E.J., M.-C.B., C.P., V.M. performed sulfides analyses (EPMA and LA-ICP-MS). M.B., E.J., M.-C.B. interpreted trace elements data with inputs from M.R., I.D.-A.; M.B., E.J., V.M. performed chlorite-mica analyses (EPMA). M.B., L.A., P.L (Pierre Lanari) interpreted the thermobarometric data with inputs from E.J., M.R., I.D.-A., M.-C.B.; M.B., E.J., P.L. (Philippe Lach), V.M. conducted U-Th-Pb monazite analyses (EPMA and LA-ICP-MS). M.B., E.J. interpreted the geochronological data with inputs from M.R., I.D.-A.; M.B. wrote the manuscript. All authors have read and agreed to the published version of the manuscript.

Funding: This work was first supported by the "Référentiel Géologique de la France" RGF-Alps Program by BRGM, which funds the doctoral grant of M. Bertauts. This work was further supported by the TelluS Program of CNRS/INSU, the IDEX-IRGA 2021, and local BQR funding. The work was mainly done in ISTerre (Université Grenoble Alpes), which is part of Labex OSUG@2020 (ANR10 LABX56). The sulfide analyses were carried out at the LA-ICP-MS laboratory of GeoRessources in Nancy, which is funded by the Labex Ressources 21 (ANR-10-LABX-21-RESSOURCES21), the Région Lorraine, and the European Community through the FEDER program.

Acknowledgments: The authors gratefully acknowledge Roger De Ascenção Guedes and Serge Fudral for their precious knowledge of the Savoie base metal occurrences and on the regional geology. We thank Laurent Truche for his precious advice, and Ahmed Nouibat for his help on MatLab software. The three anonymous reviewers helped clarifying several aspects of the paper and are sincerely acknowledged.

Conflicts of Interest: The authors declare no conflict of interest.

References

1. Meloux, J. *Alpes-Nord, Bilan Synthétique de dix Années de Prospection*; Report No. 75-RME-023-FE; BRGM: Orléans, France, 1975; p. 104.
2. Caby, R. Etude Géologique et Métallogénique du Bord Interne de la Zone Houillère et de la Bordure des Schistes Lustrés Entre Modane et la Vallée étroite (Savoie, Haut Val de Susa). Ph.D. Thesis, University of Paris, Paris, France, 1963; p. 205.

3. Rogel, P. Le Gisement de Plomb de La Plagne (Savoie)—Etude Géologique et Métallogénique—Vanoise. Ph.D. Thesis, University of Paris, Paris, France, 1961; p. 100.
4. Rogel, P. *Exemple de Gisement de Galène du Trias des Alpes. Coll. Trias de la France et des Régions Limitrophes. Mém*; BRGM: Paris, France, 1963; Volume 15, pp. 695–704.
5. Bouladon, J. Contribution à une systématique des gisements de plomb et de zinc. *Chron. Mines Rech. Min.* **1969**, *8*, 215–227.
6. Raguin, E. La mine de plomb argentifère de La Plagne (Savoie). *Ann. Des Mines* **1938**, *13*, 53–62.
7. Waline, P. La mine de La Plagne. *Miner. Ind. Rev.* **1960**, *42*, 447–460.
8. Cabrol, B. Etude Géologique et Minière du Massif des Hurtières-Chaine de Belledonne (Savoie)—Alpes Françaises. Ph.D. Thesis, University of Grenoble, Grenoble, France, 1967.
9. Ypma, P.J. Rejuvenation of Ore Deposits as Exemplified by the Belledonne Metalliferous Province. Ph.D. Thesis, University of Rennes, Rennes, France, 1963.
10. Court, P. *Etude Géologique et Métallogénique de la Basse-Maurienne (Savoie)—Alpes Françaises*; Faculté des Sciences de Grenoble: Grenoble, France, 1971.
11. Ochoa Alencastre, A. Etude Gîtologique des Minéralisations Fluorées du Massif de Rocheray, Savoie—Alpes Françaises Externes. Ph.D. Thesis, University of Claude Bernard-Lyon 1, Lyon, France, 1979.
12. Negga, H.S. Comportement de L'uranium lors des Métamorphismes tardi-Hercinien et Alpin Dans les Massifs des Aiguilles Rouges et de Belledonne (Vallorçine, Lauzière). Alpes Occidentales. Ph.D. Thesis, University of Nançy, Nancy, France, 1984.
13. Routhier, P. *Les Gisements Métallifères. Géologie et Principes de Recherche*; Masson: Paris, France, 1963; p. 1282.
14. Zhong, R.; Li, W.; Chen, Y.; Huo, H. Ore-Forming Conditions and Genesis of the Huogeqi Cu–Pb–Zn–Fe Deposit in the Northern Margin of the North China Craton: Evidence from Ore Petrologic Characteristics. *Ore Geol. Rev.* **2012**, *44*, 107–120. [CrossRef]
15. Gibson, G.M.; Hutton, L.J.; Holzschuh, J. Basin Inversion and Supercontinent Assembly as Drivers of Sediment-Hosted Pb–Zn Mineralization in the Mount Isa Region, Northern Australia. *J. Geol. Soc.* **2017**, *174*, 773–786. [CrossRef]
16. Cugerone, A.; Oliot, E.; Chauvet, A.; Gavaldà Bordes, J.; Laurent, A.; Le Goff, E.; Cenki-Tok, B. Structural Control on the Formation of Pb-Zn Deposits: An Example from the Pyrenean Axial Zone. *Minerals* **2018**, *8*, 489. [CrossRef]
17. Cugerone, A.; Roger, F.; Cenki, B.; Oliot, E.; Paquette, J.-L. Variscan U-Th-Pb Age for Stratabound Pb-Zn Mineralization in the Bossòst Dome (Pyrenean Axial Zone). *Ore Geol. Rev.* **2021**, *139*, 104503. [CrossRef]
18. Cave, B.; Perkins, W.; Lilly, R. Linking Uplift and Mineralisation at the Mount Novit Zn-Pb-Ag Deposit, Northern Australia: Evidence from Geology, U–Pb Geochronology and Sphalerite Geochemistry. *Geosci. Front.* **2022**, *13*, 101347. [CrossRef]
19. Gasquet, D.; Bertrand, J.-M.; Paquette, J.-L.; Lehmann, J.; Ratzov, G.; De Ascenção Guedes, R.; Tiepolo, M.; Boullier, A.-M.; Scaillet, S.; Nomade, S. Miocene to Messinian deformation and hydrothermal activity in a pre-Alpine basement massif of the French western Alps: New U-Th-Pb and argon ages from the Lauzière Massif. *Bull. Soc. Géol. Fr.* **2010**, *181*, 227–241. [CrossRef]
20. Grand'Homme, A.; Janots, E.; Bosse, V.; Seydoux-Guillaume, A.M.; De Ascenção Guedes, R. Interpretation of U-Th-Pb in-situ ages of hydrothermal monazite-(Ce) and xenotime-(Y): Evidence from a large-scale regional study in clefts from the western alps. *Mineral. Petrol.* **2016**, *110*, 787–807. [CrossRef]
21. Gnos, E.; Mullis, J.; Ricchi, E.; Bergemann, C.A.; Janots, E.; Berger, A. Episodes of fissure formation in the Alps: Connecting quartz fluid inclusion, fissure monazite age, and fissure orientation data. *Swiss J. Geosci.* **2021**, *114*, 14. [CrossRef] [PubMed]
22. Guillot, F. Géologie de l'Antépermien de Vanoise Septentrionale (Zone Briançonnaise Interne, Savoie, France). Ph.D. Thesis, University of Lille, Lille, France, 1987.
23. Schmid, S.M.; Fügenschuh, B.; Kissling, E.; Schuster, R. Tectonic map and overall architecture of the Alpine Orogen. *Eclogae Geol. Helv.* **2004**, *97*, 93–117. [CrossRef]
24. Ceriani, S.; Fügenschuh, B.; Schmid, S.M. Multi-stage thrusting at the "Penninic Front" in the Western Alps between Mont Blanc and Pelvoux massifs. *Int. J. Earth Sci.* **2001**, *90*, 685–702. [CrossRef]
25. Barré, G.; Strzerzynski, P.; Michels, R.; Guillot, S.; Cartigny, P.; Thomassot, E.; Lorgeoux, C.; Assayag, N.; Truche, L. Tectono-metamorphic evolution of an evaporitic décollement as recorded by mineral and fluid geochemistry: The "Nappe Des Gypses" (Western Alps) case study. *Lithos* **2020**, *358–359*, 105419. [CrossRef]
26. Giorgis, D.; Thélin, P.; Stampfli, G.; Bussy, F. The Mont-Mort metapelites:Variscan metamorphism and geodynamic context (Briançonnais basement, Western Alps, Switzerland). *Schweiz. Mineral. Petrogr. Mitt.* **1999**, *79*, 381–398.
27. Guillot, F.; Schaltegger, U.; Bertrand, J.M.; Deloule, É.; Baudin, T. Zircon U–Pb geochronology of Ordovician magmatism in the polycyclic Ruitor Massif (Internal W Alps). *Int. J. Earth Sci.* **2002**, *91*, 964–978. [CrossRef]
28. Fabre, J. Contribution à l'étude de la Zone Houillère en Maurienne et en Tarentaise (Alpes de Savoie). Ph.D. Thesis, University of Paris, Paris, France, 1958.
29. Lanari, P.; Guillot, S.; Schwartz, S.; Vidal, O.; Tricart, P.; Riel, N.; Beyssac, O. Diachronous evolution of the alpine continental subduction wedge: Evidence from P–T estimates in the Briançonnais Zone Houillère (France—Western Alps). *J. Geodyn.* **2012**, *56–57*, 39–54. [CrossRef]
30. Ellenberger, F. *Etude géologique du pays de Vanoise. Mémoires du Service de la Carte Géologique de la France*; Imprimerie Nationale: Paris, France, 1958; p. 561.
31. Goffé, B.; Schwartz, S.; Lardeaux, J.M.; Bousquet, R. Explanatory notes to the map: Metamorphic structure of the Alps Western and Ligurian Alps. *Mitt. Österr. Miner. Ges.* **2004**, *149*, 125–144.

32. Bousquet, R.; Oberhänsli, R.; Goffé, B.; Wiederkehr, M.; Koller, F.; Schmid, S.M.; Schuster, R.; Engi, M.; Berger, A.; Martinotti, G. Metamorphism of metasediments at the scale of an orogen: A key to the Tertiary geodynamic evolution of the Alps. *Geol. Soc. Spec. Publ.* **2008**, *298*, 393–411. [CrossRef]
33. Bertrand, J.M.; Aillères, L.; Gasquet, D. The Pennine Front zone in Savoie (Western Alps), a review and new interpretations from the Zone Houillère Briançonnaise. *Eclogae Geol. Helv.* **1996**, *89*, 297–320. [CrossRef]
34. Strzerzynski, P.; Guillot, S.; Leloup, P.H.; Arnaud, N.; Vidal, O.; Ledru, P.; Courrioux, G.; Darmendrail, X. Tectono-metamorphic evolution of the Briançonnais zone (Modane-Aussois and Southern Vanoise units, Lyon Turin transect, Western Alps). *J. Geodyn.* **2012**, *56–57*, 55–75. [CrossRef]
35. Ganne, J. Les Dômes de Socles HP-BT dans le Domaine Pennique des Alpes Nord-Occidentales (Massifs d'Ambin et de Vanoise Sud): Modalités de Leur Exhumation. Ph.D. Thesis, University of Savoie, Chambéry, France, 2003.
36. Gerber, W. Evolution Tectono-Métamorphique du Briançonnais Interne (Alpes Occidentales, Massifs de Vanoise Sud et d'Ambin): Comportement du Socle et de sa Couverture Dans un Contexte de Subduction Continentale Profonde. Ph.D. Thesis, University of Pierre et Marie Curie (Paris 6), Paris, France, 2008.
37. Ganne, J.; Bertrand, J.-M.; Fudral, S.; Marquer, D.; Vidal, O. Structural and metamorphic evolution of the Ambin massif (Western Alps): Toward a new alternative exhumation model for the Briançonnais domain. *Bull. Soc. Géol. Fr.* **2007**, *178*, 437–458. [CrossRef]
38. Platt, T.P.; Lister, G.S. Structural history of high-pressure metamorphic rocks in the southern Vanoise massif, French Alps, and their relation to Alpine tectonic events. *J. Struct. Geol.* **1985**, *7*, 19–35. [CrossRef]
39. Freeman, S.R.; Inger, S.; Butler, R.W.H.; Cliff, R.A. Dating deformation using Rb-Sr in white mica: Greenschist facies deformation ages from the Entrelor shear zone, Italian Alps. *Tectonics* **1997**, *16*, 57–76. [CrossRef]
40. Gabalda, S. *Processus d'exhumation dans les Alpes Occidentales: Modélisation Géométrique et Reconstitution Géodynamique sur la Transversale Chartreuse-Maurienne, une Approche Multi-Échelle*; Ecole des Mines: Paris, France, 2008.
41. Bucher, S.; Schmid, S.M.; Bousquet, R.; Fugenschuh, B. Late-stage deformation in a collisional orogen (Western Alps): Nappe refolding, back-thrusting or normal faulting? *Terra Nova* **2003**, *15*, 109–117. [CrossRef]
42. Lanari, P.; Rolland, Y.; Schwartz, S.; Vidal, O.; Guillot, S.; Tricart, P.; Dumont, T. P-T-t estimation of deformation in low-grade quartz-feldspar-bearing rocks using thermodynamic modelling and 40Ar/39Ar dating techniques: Example of the Plan-de-Phasy shear zone unit (Briançonnais Zone, Western Alps). *Terra Nova* **2014**, *26*, 130–138. [CrossRef]
43. Guillot, F. La Vallée du Ponturin (Vanoise Septentrionale, Alpes Françaises). Master's Thesis, University of Paris, Paris, France, 1982.
44. BRGM. *Les Gisements de Pb-Zn Français. (Situation en 1977)*; Report No: RR-41430-FR-02; BRGM: Paris, France, 1977; p. 278.
45. Gimard, J.; Gimard, G. *Mine de Plomb Argentifère (Savoie)*; Monde et Minéraux: Paris, France, 1985; pp. 10–14.
46. Tachat, T. *Mine de Plomb Argentifère*; BRGM: Paris, France, 1861; pp. 1–14.
47. Gimard, J.; Gimard, G. *Mines de Plomb Argentifère (Savoie)*; Monde et Minéraux: Paris, France, 1986; pp. 42–43.
48. Passchier, C.W.; Trouw, R.A. *Microtectonics*; Springer Science & Business Media: Berlin, Germany, 2005; p. 366. ISBN 3-540-64003-7.
49. Belissont, R.; Boiron, M.-C.; Luais, B.; Cathelineau, M. LA-ICP-MS analyses of minor and trace elements and bulk Ge isotopes in zoned Ge-rich sphalerites from the Noailhac—Saint-Salvy deposit (France): Insights into incorporation mechanisms and ore deposition processes. *Geochim. Cosmochim. Acta* **2014**, *126*, 518–540. [CrossRef]
50. Wilson, S.A.; Ridley, W.I.; Koenig, A.E. Development of sulfide calibration standards for the laser ablation inductively-coupled plasma mass spectrometry technique. *J. Anal. At. Spectrom.* **2002**, *17*, 406–409. [CrossRef]
51. Paton, C.; Hellstrom, J.; Paul, B.; Woodhead, J.; Hergt, J. Iolite: Freeware for the visualisation and processing of mass spectrometric data. *J. Anal. At. Spectrom.* **2011**, *26*, 2508. [CrossRef]
52. Longerich, H.P.; Jackson, S.E.; Gunther, D. Inter-Laboratory Note. Laser Ablation Inductively Coupled Plasma Mass Spectrometric Transient Signal Data Acquisition and Analyte Concentration Calculation. *J. Anal. At. Spectrom.* **1996**, *11*, 899–904. [CrossRef]
53. De Andrade, V.; Vidal, O.; Lewin, E.; O'Brien, P.; Agard, P. Quantification of electron microprobe compositional maps of rock thin sections: An optimized method and examples. *J. Metamorph. Geol.* **2006**, *24*, 655–668. [CrossRef]
54. Lanari, P.; Vidal, O.; De Andrade, V.; Dubacq, B.; Lewin, E.; Grosch, E.G.; Schwartz, S. XMapTools: A MATLAB©-based program for electron microprobe X-ray image processing and geothermobarometry. *Comput. Geosci.* **2014**, *62*, 227–240. [CrossRef]
55. Lanari, P.; Vho, A.; Bovay, T.; Airaghi, L.; Centrella, S. Quantitative compositional mapping of mineral phases by electron probe micro-analyser. *Geol. Soc. Lond. Spec. Publ.* **2019**, *478*, 39–63. [CrossRef]
56. Bourdelle, F.; Cathelineau, M. Low-temperature chlorite geothermometry: A graphical representation based on a T–R2+ –Si diagram. *Eur. J. Mineral.* **2015**, *27*, 617–626. [CrossRef]
57. Vidal, O.; Lanari, P.; Munoz, M.; Bourdelle, F.; De Andrade, V. Deciphering temperature, pressure and oxygen-activity conditions of chlorite formation. *Clay Miner.* **2016**, *51*, 615–633. [CrossRef]
58. Parra, T.; Vidal, O.; Agard, P. A thermodynamic model for Fe–Mg dioctahedral K white micas using data from phase-equilibrium experiments and natural pelitic assemblages. *Contrib. Mineral. Petrol.* **2002**, *143*, 706–732. [CrossRef]
59. Dubacq, B.; Vidal, O.; De Andrade, V. Dehydration of dioctahedral aluminous phyllosilicates: Thermodynamic modelling and implications for thermobarometric estimates. *Contrib. Mineral. Petrol.* **2010**, *159*, 159–174. [CrossRef]
60. Vidal, O.; Parra, T.; Trottet, F. A thermodynamic model for Fe-Mg aluminous chlorite using data from phase equilibrium experiments and natural pelitic assemblages in the 100 to 600 °C, 1 to 25 kb range. *Am. J. Sci.* **2001**, *301*, 557–592. [CrossRef]

61. Vidal, O.; Parra, T.; Vieillard, P. Thermodynamic properties of the Tschermak solid solution in Fe-Chlorite: Application to natural examples and possible role of oxidation. *Am. Mineral.* **2005**, *90*, 347–358. [CrossRef]
62. Vidal, O.; De Andrade, V.; Lewin, E.; Munoz, M.; Parra, T.; Pascarelli, S. P-T-Deformation-Fe3+/Fe2+ mapping at the thin section scale and comparison with XANES mapping: Application to a garnet-bearing metapelite from the Sambagawa metamorphic belt (Japan). *J. Metamorph. Geol.* **2006**, *24*, 669–683. [CrossRef]
63. Lanari, P. Micro-Cartographie P-T-ε Dans les roches Métamorphiques. Applications aux Alpes et à l'Himalaya. Ph.D. Thesis, University of Grenoble, Grenoble, France, 2012.
64. Cathelineau, M. Cation site occupancy in chlorites and illites as a function of emperature. *Clay Miner.* **1988**, *23*, 471–485. [CrossRef]
65. Seydoux-Guillaume, A.-M.; Montel, J.-M.; Bingen, B.; Bosse, V.; de Parseval, P.; Paquette, J.-L.; Janots, E.; Wirth, R. Low-temperature alteration of monazite: Fluid mediated coupled dissolution–precipitation, irradiation damage, and disturbance of the U–Pb and Th–Pb chronometers. *Chem. Geol.* **2012**, *330–331*, 140–158. [CrossRef]
66. Villa-Vialaneix, N.; Montel, J.M.; Seydoux-Guillaume, A.M. NiLeDAM: Monazite Datation for the NiLeDAM Team. R Package Version 0.1. 2013. Available online: http://niledam.r-forge.r-project.org (accessed on 30 July 2019).
67. Tomascak, P.B.; Krogstad, E.J.; Walker, R.J. U-Pb Monazite geochronology of granitic rocks from Maine: Implications for late Paleozoic tectonics in the northern Appalachians. *J. Geol.* **1996**, *104*, 185–195. [CrossRef]
68. Schulz, B.; Brätz, H.; Bombach, K.; Krenn, E. In situ Th-Pb dating of monazite by 266 nm laser ablation and ICP-MS with a single collector, and its control by EMP analysis. *J. Geol. Sci.* **2007**, *35*, 377–392.
69. Vermeesch, P. IsoplotR: A free and open toolbox for geochronology. *Geosci. Front.* **2018**, *9*, 1479–1493. [CrossRef]
70. Whitney, D.L.; Evans, B.W. Abbreviations for Names of Rock-Forming Minerals. *Am. Mineral.* **2010**, *95*, 185–187. [CrossRef]
71. George, L.; Cook, N.J.; Ciobanu, C.L.; Wade, B.P. Trace and Minor Elements in Galena: A Reconnaissance LA-ICP-MS Study. *Am. Mineral.* **2015**, *100*, 548–569. [CrossRef]
72. Moëlo, Y.; Makovicky, E.; Mozgova, N.N.; Jambor, J.L.; Cook, N.; Pring, A.; Paar, W.; Nickel, E.H.; Graeser, S.; Karup-Møller, S.; et al. Sulfosalt systematics: A review. Report of the sulfosalt sub-committee of the IMA commission on ore mineralogy. *Eur. J. Mineral.* **2008**, *20*, 7–62. [CrossRef]
73. Biagioni, C.; George, L.L.; Cook, N.J.; Makovicky, E.; Moëlo, Y.; Pasero, M.; Sejkora, J.; Stanley, C.J.; Welch, M.D.; Bosi, F. The tetrahedrite group: Nomenclature and classification. *Am. Mineral.* **2020**, *105*, 109–122. [CrossRef]
74. George, L.; Cook, N.; Ciobanu, C. Minor and trace elements in natural tetrahedrite-tennantite: Effects on element partitioning among base metal sulphides. *Minerals* **2017**, *7*, 17. [CrossRef]
75. Masci, L. Cristallochimie du fer dans les Chlorites Métamorphiques: Approche Analytique Multiéchelle, Expérimentale, et Implications Pétrologiques. Ph.D. Thesis, Sorbonne University, Paris, France, 2019.
76. Inoue, A.; Meunier, A.; Patrier-Mas, P.; Rigault, C.; Beaufort, D.; Vieillard, P. Application of chemical geothermometry to low-temperature trioctahedral chlorites. *Clays Clay Miner.* **2009**, *57*, 371–382. [CrossRef]
77. Bourdelle, F.; Parra, T.; Chopin, C.; Beyssac, O. A new chlorite geothermometer for diagenetic to low-grade metamorphic conditions. *Contrib. Mineral. Petrol.* **2013**, *165*, 723–735. [CrossRef]
78. Stacey, J.S.; Kramers, J.D. Approximation of terrestrial lead isotope evolution by a two-stage model. *Earth Planet. Sci. Lett.* **1975**, *26*, 207–221.
79. Cumming, G.L.; Richards, J.R. Ore lead isotope ratios in a continuously changing Earth. *Earth Planet. Sci. Lett.* **1975**, *28*, 155–171. [CrossRef]
80. Rossi, M.; Rolland, Y.; Vidal, O.; Cox, S.F. Geochemical Variations and Element Transfer during Shear-Zone Development and Related Episyenites at Middle Crust Depths: Insights from the Mont Blanc Granite (French—Italian Alps). *Geol. Soc. Spec. Publ.* **2005**, *245*, 373–396. [CrossRef]
81. Cenki-Tok, B.; Darling, J.R.; Rolland, Y.; Dhuime, B.; Storey, C.D. Direct Dating of Mid-Crustal Shear Zones with Synkinematic Allanite: New in Situ U-Th-Pb Geochronological Approaches Applied to the Mont Blanc Massif. *Terra Nova* **2014**, *26*, 29–37. [CrossRef]
82. Cook, N.J.; Klemd, R.; Okrusch, M. Sulphide Mineralogy, metamorphism and deformation in the matchless massive sulphide deposit, Namibia. *Miner. Depos.* **1994**, *29*, 1–15. [CrossRef]
83. Gu, L.; Zheng, Y.; Tang, X.; Zaw, K.; Della-Pasque, F.; Wu, C.; Tian, Z.; Lu, J.; Ni, P.; Li, X.; et al. Copper, gold and silver enrichment in ore mylonites within massive sulphide orebodies at Hongtoushan VHMS deposit, N.E. China. *Ore Geol. Rev.* **2007**, *30*, 1–29. [CrossRef]
84. Turlin, F.; Eglinger, A.; Vanderhaeghe, O.; André-Mayer, A.-S.; Poujol, M.; Mercadier, J.; Bartlett, R. Synmetamorphic Cu remobilization during the Pan-African orogeny: Microstructural, petrological and geochronological data on the kyanite-micaschists hosting the Cu(–U) Lumwana deposit in the Western Zambian copperbelt of the Lufilian belt. *Ore Geol. Rev.* **2016**, *75*, 52–75. [CrossRef]
85. Zheng, Y.; Wang, Y.; Chen, H.; Lin, Z.; Hou, W.; Li, D. Micro-textural and fluid inclusion data constraints on metallic remobilization of the Ashele VMS Cu-Zn deposit, Altay, NW China. *J. Geochem. Explor.* **2016**, *171*, 113–123. [CrossRef]
86. Janots, E.; Negro, F.; Brunet, F.; Goffé, B.; Engi, M.; Bouybaouène, M.L. Evolution of the REE mineralogy in HP–LT metapelites of the Sebtide complex, rif, Morocco: Monazite stability and geochronology. *Lithos* **2006**, *87*, 214–234. [CrossRef]
87. Wing, B.A.; Ferry, J.M.; Harrison, T.M. Prograde destruction and formation of monazite and allanite during contact and regional metamorphism of pelites: Petrology and geochronology. *Contrib. Mineral. Petrol.* **2003**, *145*, 228–250. [CrossRef]

88. Rasmussen, B.; Fletcher, I.R.; Muhling, J.R. In situ U–Pb dating and element mapping of three generations of monazite: Unravelling cryptic tectonothermal events in low-grade terranes. *Geochim. Cosmochim. Acta* **2007**, *71*, 670–690. [CrossRef]
89. Janots, E.; Engi, M.; Berger, A.; Allaz, J.; Schwarz, J.-O.; Spandler, C. Prograde metamorphic sequence of REE minerals in pelitic rocks of the central Alps: Implications for allanite–monazite–xenotime phase relations from 250 to 610 °C. *J. Metamorph. Geol.* **2008**, *26*, 509–526. [CrossRef]
90. Seybold, L.; Trepmann, C.A.; Janots, E. A ductile extensional shear zone at the contact area between HP-LT metamorphic units in the Talea Ori, central Crete, Greece: Deformation during early stages of exhumation from peak metamorphic conditions. *Int. J. Earth Sci.* **2019**, *108*, 213–227. [CrossRef]
91. Čopjaková, R.; Novák, M.; Franců, E. Formation of authigenic monazite-(Ce) to monazite-(Nd) from upper Carboniferous graywackes of the Drahany upland: Roles of the chemical composition of host rock and burial temperature. *Lithos* **2011**, *127*, 373–385. [CrossRef]
92. Boulter, C.A.; Fotios, M.G.; Phillips, G.N. The golden mile, Kalgoorlie; a giant gold deposit localized in ductile shear zones by structurally induced infiltration of an auriferous metamorphic fluid. *Econ. Geol.* **1987**, *82*, 1661–1678. [CrossRef]
93. Gratier, J.-P.; Dysthe, D.K.; Renard, F. The role of pressure solution creep in the ductility of the Earth's upper crust. *Adv. Geophys.* **2013**, *54*, 47–179.
94. Renard, F.; Brosse, E.; Gratier, J.P. The different processes involved in the mechanism of pressure solution in quartz-rich rocks and their interactions. *Quartz Cem. Sandstones* **2000**, *29*, 67–78.
95. Sibson, R.H. Implications of fault-valve behaviour for rupture nucleation and recurrence. *Tectonophysics* **1992**, *211*, 283–293. [CrossRef]
96. Cox, S.F. The application of failure mode diagrams for exploring the roles of fluid pressure and stress states in controlling styles of fracture-controlled permeability enhancement in faults and shear zones. *Geofluids* **2010**, *10*, 217–233. [CrossRef]
97. Renard, F.; Gratier, J.-P.; Jamtveit, B. Kinetics of crack-sealing, intergranular pressure solution, and compaction around active faults. *J. Struct. Geol.* **2000**, *22*, 1395–1407. [CrossRef]